

## THE ROLE OF COSMIC RAY TRANSPORT IN SHAPING THE SIMULATED CIRCUMGALACTIC MEDIUM

IRYNA S. BUTSKY AND THOMAS R. QUINN

Astronomy Department, University of Washington, Box 351580, Seattle, WA 98195-1580, USA

*Draft version October 24, 2018*

### ABSTRACT

The majority of galactic baryons reside outside of the galactic disk in the diffuse gas known as the circumgalactic medium (CGM). While state-of-the-art simulations excel at reproducing galactic disk properties, many struggle to drive strong galactic winds or to match the observed ionization structure of the CGM using only thermal supernova feedback. To remedy this, recent studies have invoked non-thermal cosmic ray (CR) stellar feedback prescriptions. However, numerical schemes of CR transport are still poorly constrained. We explore how the choice of CR transport affects the multiphase structure of the simulated CGM. We implement anisotropic CR physics in the astrophysical simulation code, ENZO and simulate a suite of isolated disk galaxies with varying prescriptions for CR transport: isotropic diffusion, anisotropic diffusion, and streaming. We find that all three transport mechanisms result in strong, metal-rich outflows but differ in the temperature and ionization structure of their CGM. Isotropic diffusion results in a spatially uniform, warm CGM that underpredicts the column densities of low-ions. Anisotropic diffusion develops a reservoir of cool gas that extends further from the galactic center, but disperses rapidly with distance. CR streaming projects cool gas out to radii of 200 kpc, supporting a truly multiphase medium. In addition, we find that streaming is less sensitive to changes in constant parameter values like the CR injection fraction, transport velocity, and resolution than diffusion. We conclude that CR streaming is a more robust implementation of CR transport and motivate the need for detailed parameter studies of CR transport.

*Subject headings:* Galaxies: evolution, halo — ISM: cosmic rays, jets and outflows — ISM: jets and outflows — Methods: numerical simulations

### 1. INTRODUCTION

The majority of baryons in galactic halos, including the majority of metals, reside in the circumgalactic medium (CGM) of galaxies (Werk et al. 2013, 2014). Loosely defined, the CGM refers to the diffuse, multiphase gas that extends to the virial radius of galaxies. The CGM is shaped by the interplay between outflows from the star-forming disk and inflows from the pristine intergalactic medium (IGM) and provides constraints to theories of galaxy formation and evolution.

Early theoretical works predicted the existence of the CGM as a by-product of the interactions between cooling and accretion during galaxy formation (Binney 1977; Rees & Ostriker 1977; Silk 1977). Due to its low density, the CGM is extremely difficult to observe directly in emission. Instead, recent observations, such as those taken with The Cosmic Origins Spectrograph (COS) (Green et al. 2012) on board the Hubble Space Telescope (HST), have studied the CGM through absorption lines in quasar spectra that intersect the halos of galaxies along the line-of-sight. Using the quasar absorption method, different groups have greatly advanced our knowledge of the CGM both in high-redshift (e.g. Steidel et al. 2010; Rudie et al. 2012; Turner et al. 2014), and low-redshift (e.g. Chen et al. 2010; Gauthier et al. 2010; Kacprzak et al. 2010; Bordoloi et al. 2011; Prochaska et al. 2011; Tumlinson et al. 2011; Nielsen et al. 2013; Stocke et al. 2013; Werk et al. 2013; Zhang et al. 2016) galaxies. Today, we understand the CGM to have an intricate and complex temperature, density, and kinematic structure that is shaped by galactic outflows.

Simulations play an integral role in understanding the physical processes that govern galactic outflows by allowing astronomers to perform experiments testing the validity of different feedback prescriptions. The success of a simulation has traditionally been marked by its ability to reproduce observed

galactic disk properties, such as the morphology, Tully-Fisher relation, and star formation rate density (Schaye et al. 2010; Davé et al. 2011; Puchwein & Springel 2013; Stinson et al. 2013; Christensen et al. 2014). Requiring that simulations also match the observed structure of the CGM will place strong additional constraints to stellar feedback models.

One such constraint is that stellar feedback must drive galactic outflows that carry a substantial amount of metals along with the gas they expel. Although metals are produced within galactic disks, galaxies retain only  $\sim 20\text{--}25\%$  of these metals in their stars and ISM (Peebles et al. 2014). Data from the Sloan Digital Sky Survey suggest that metals have been lost to outflows (Tremonti et al. 2004). Since galaxies have very low metallicities at early cosmic times ( $z > 3$ ), the metals ejected by supernovae serve as excellent tracers of outflowing material and can be used to make predictions for future observations.

These outflows must not only enrich the CGM but also reproduce its multiphase ionization structure. For example, the CGM of galaxies at low redshift contains a substantial amount of metal-enriched, cool gas at  $10^4\text{--}10^5\text{K}$  (Werk et al. 2013, 2014). However, cooling times of  $\simeq 10^5\text{K}$  gas are very short compared to galactic timescales, and it is unclear how this material survives in such abundance. The data seem to imply an additional unknown source of non-thermal pressure that supports the warm gas against condensation.

Recent studies have investigated various types of thermal wind-launching mechanisms, including radiation pressure from massive stars (Kim et al. 2011; Murray et al. 2011; Hopkins et al. 2012; Sharma & Nath 2012; Wise et al. 2012), thermal supernova feedback (Abadi et al. 2003; Joung et al. 2009; Hummels & Bryan 2012; Creasey et al. 2013), kinetic supernova feedback (Hopkins et al. 2012; Springel & Hernquist 2003; Agertz et al. 2013), supernova superbubble mod-

els, (Keller et al. 2015, 2016), and subgrid models tuned to generate strong outflows (e.g. Springel & Hernquist 2003; Stinson et al. 2006; Oppenheimer & Davé 2006; Governato et al. 2012)). However, many of these feedback prescriptions still struggle to produce sufficiently strong galactic outflows. Those that do succeed in expelling gas from the galactic disk underpredict the observed column densities of H I, O VI, and low ions in the CGM. (Hummels et al. 2013; Marasco et al. 2015; Fielding et al. 2017; Gutcke et al. 2017). This discrepancy is amplified in massive galaxies for which thermal supernova feedback also struggles to quench star formation (Pontzen et al. 2013). In such galaxies, feedback from active galactic nuclei (AGN) is often invoked to regulate the baryon cycling process (e.g. Suresh et al. 2015; Tremmel et al. 2017; Oppenheimer et al. 2018). Although AGN help recreate some observable properties for massive galaxies, they cannot account for discrepancies in galaxies (such as the Milky Way) that host a small supermassive black hole (SMBH) at their core. It is likely that the missing key is a non-thermal component.

Cosmic rays (CRs) are charged particles that have been accelerated to relativistic speeds in shocks (e.g. SNe Ackermann et al. 2013, structure formation shocks Pfrommer et al. 2008 radio-loud AGN McNamara & Nulsen 2007) and are observed to be roughly in equilibrium with the thermal and magnetic pressures in our galaxy (Boulares & Cox 1990). Due to past computational constraints, CRs have only recently been included in 3-D hydrodynamical simulations of galactic structure. These simulations have shown that CR feedback drives strong, mass-loaded outflows and suppresses star formation (e.g. Miniati et al. 2001; Enßlin et al. 2007; Jubelgas et al. 2008; Socrates et al. 2008; Uhlig et al. 2012; Vazza et al. 2012; Booth et al. 2013; Salem & Bryan 2014; Girichidis et al. 2016; Simpson et al. 2016; Samui et al. 2018). Furthermore, CRs provide pressure support to the thermal gas, which may explain the presence of the observed structures in the CGM that appear to be out of thermal equilibrium.

Salem et al. (2016) were the first to show that stellar feedback models that included CR energy were better at matching COS-Halos data for low-ion column densities than those with purely thermal feedback. However, these results depended on the choice of a constant diffusion coefficient, which is only loosely constrained by observations. Furthermore, their simulations neglected magnetic fields, which are crucial for accurate modeling of CR transport. Traditionally, implementations of CR transport have been separated into two approximations: diffusion and streaming. Although both approaches have been successful at driving galactic outflows, the strength and mass-loading factor of CR driven winds depends on the invoked transport mechanism (Ruszkowski et al. 2017; Wiener et al. 2017).

In this work, we investigate the role of different CR transport prescriptions in shaping the multiphase structure of the CGM. This paper is structured as follows. In §2, we describe the implementation of CR physics in *ENZO*. In §3, we describe the simulation suite and the relevant initial conditions and physical modules used in our isolated disk setup. We present our results in §4, focusing on the generated outflows, temperature structure, and column densities of the different galaxy models. We outline the qualitative differences between CR diffusion and streaming and discuss future prospects in §5. Finally, we provide a summary of our work in §6.

In the following section, we describe our implementation of the CR fluid into the different Riemann solvers in the adaptive mesh refinement (AMR) magnetohydrodynamics (MHD) simulation code *ENZO*. Our implementation builds on the work of Salem & Bryan (2014), which described the integration of a CR fluid in the *ZEUS* finite-difference solver (Stone & Norman 1992). Because the current implementation of the *ZEUS* solver in the public version of *ENZO* doesn't support MHD, the primary advantage of our work is the ability to model the interaction of CRs with magnetic field lines. In §2.1, we describe the new set of conservation equations. In §2.2 and §2.3, we describe the algorithm for anisotropic CR streaming and diffusion. In §2.4 we discuss our approach for avoiding unphysical values of CR energy.

### 2.1. Cosmic Ray Fluid

As an Eulerian code, *ENZO* models gas as a fluid moving through grid cells that are fixed in space. At every timestep, *ENZO* advances the state of the fluid in the simulation by numerically approximating a solution to the equations below. These equations encompass the conservation of mass (Equation 1), conservation of momentum (Equation 2), the induction equation (Equation 3), and the energy equation (Equation 4). In simplified terms, these equations assert that the change over time in the value of a given conserved quantity in one cell (the  $\frac{\partial}{\partial t}$  term) is equal to the flux of that conserved quantity through the boundaries of that cell (the  $\nabla \cdot ()$  term). Source terms, which encompass both energy gains and losses (for example, an injection of CR energy after a supernova explosion) appear on the right-hand-side of the equality. Traditionally, the evolution of thermal gas is encompassed in Equations 1 - 4 (setting the cosmic ray pressure term,  $P_c$  to zero). We model the evolution of CRs as an additional ultra-relativistic proton fluid with adiabatic index  $\gamma_c = 4/3$  (Jun et al. 1994; Drury & Falle 1986) in Equation 5.

$$\frac{\partial \rho}{\partial t} + \nabla \cdot (\rho \mathbf{v}) = 0 \quad (1)$$

$$\frac{\partial (\rho \mathbf{v})}{\partial t} + \nabla \cdot (\rho \mathbf{v} \mathbf{v}^T + P_g + P_c) = -\rho \nabla \Phi \quad (2)$$

$$\frac{\partial \mathbf{B}}{\partial t} + \nabla \cdot (\mathbf{B} \mathbf{v}^T - \mathbf{v} \mathbf{B}^T) = \mathbf{0} \quad (3)$$

$$\frac{\partial \varepsilon_g}{\partial t} + \nabla \cdot (\mathbf{v} \varepsilon_g) = -P_g \nabla \cdot \mathbf{v} + H_c + \Gamma_g + \Lambda_g \quad (4)$$

$$\frac{\partial \varepsilon_c}{\partial t} + \nabla \cdot \mathbf{F}_c = -P_c \nabla \cdot \mathbf{v} - H_c + \Gamma_c + \Lambda_c. \quad (5)$$

$$\mathbf{F}_c = \mathbf{v} \varepsilon_c + \mathbf{v}_s (\varepsilon_c + P_c) - \kappa_\varepsilon \mathbf{b} (\mathbf{b} \cdot \nabla \varepsilon_c) \quad (6)$$

Here, we define  $\Phi$  to be the gravitational potential (where  $\nabla^2 \Phi = 4\pi \mathbf{G} \rho_{tot}$ ),  $\rho_{tot}$  to be the total density, and  $\rho$ ,  $\mathbf{v}$  to be the gas density and velocity.  $\mathbf{B}$  is the magnetic field strength, and  $\mathbf{b} = \mathbf{B}/|\mathbf{B}|$  is the magnetic field direction. The superscript T denotes the vector transpose. The internal gas pressure,  $P_g$  is related to the internal thermal energy density  $\varepsilon_g = (\gamma_g - 1)P_g$ , where  $\gamma_g = 5/3$ . Similarly, the CR pressure is related to the CR energy density,  $\varepsilon_c = (\gamma_c - 1)P_c$ , with  $\gamma_c = 4/3$ . From here on out, we use the subscript 'g' to refer to properties of the thermal gas, and the subscript 'c' to refer to properties of the CR fluid. We model the diffusion coefficient,  $\kappa_\varepsilon$  as a

TABLE 1  
SIMULATION PARAMETERS

Run ID	Min. grid size (pc)	CR parameters				
		$f_c$	Transport Mode	$\kappa_\varepsilon [\times 10^{28} \text{ cm}^2/\text{s}]$	$f_s$	$H_c$
NCR	<b>160</b>	-	<b>no CRs</b>	-	-	<b>no</b>
	320	-	no CRs	-	-	no
ADV	<b>160</b>	<b>0.1</b>	<b>advection only</b>	<b>0</b>	-	<b>no</b>
	320	0.01	advection only	0	-	no
	320	0.1	advection only	0	-	no
	320	0.3	advection only	0	-	no
ISOD	<b>160</b>	<b>0.1</b>	<b>isotropic diffusion</b>	<b>3</b>	-	<b>no</b>
	320	0.01	isotropic diffusion	3	-	no
	320	0.1	isotropic diffusion	3	-	no
	320	0.3	isotropic diffusion	3	-	no
	320	0.1	isotropic diffusion	1	-	no
<sup>a</sup> ANISD	<b>160</b>	<b>0.1</b>	<b>anisotropic diffusion</b>	<b>3</b>	-	<b>no</b>
	320	0.01	anisotropic diffusion	3	-	no
	320	0.1	anisotropic diffusion	3	-	no
	320	0.1	anisotropic diffusion	10	-	no
	320	0.3	anisotropic diffusion	3	-	no
	320	0.1	anisotropic diffusion	1	-	no
ANISDH	<b>160</b>	<b>0.1</b>	<b>anisotropic diffusion</b>	<b>3</b>	-	<b>yes</b>
	320	0.1	anisotropic diffusion	3	-	yes
STREAM	<b>160</b>	<b>0.1</b>	<b>streaming</b>	-	<b>4</b>	<b>yes</b>
	160	0.1	streaming	-	1	yes
	320	0.01	streaming	-	4	yes
	320	0.1	streaming	-	1	yes
	320	0.1	streaming	-	2	yes
	320	0.1	streaming	-	4	yes
	320	0.3	streaming	-	4	yes

<sup>a</sup>A summary of the simulation initial conditions. The run ID and the corresponding boldface entries describe the fiducial runs discussed in depth throughout this paper. The fiducial runs differ from each other only by the invoked CR transport mechanism. We deviate from the fiducial runs by changing the resolution, the fraction of supernova energy injected as CRs ( $f_c$ ), the diffusion coefficient ( $\kappa_\varepsilon$ ), the streaming factor ( $f_s$ ), and including the CR heating term ( $H_c$ ). Figure 11 compares the effect of these variables on the CR pressure distribution in the CGM.

constant, which is observationally constrained to be on the order of  $\kappa_\varepsilon \simeq 10^{28} \text{ cm}^2 \text{ s}^{-1}$  (Ptuskin et al. 2006; Strong & Moskalenko 1998; Tabatabaei et al. 2013). Although we neglect CR transport perpendicular to the magnetic field, it could have observable effects (Kumar & Eichler 2014).  $\Gamma$  and  $\Lambda$  are energy source and sink terms respectively. In our simulations, the source of CR energy is supernova events. We do not implement hadronic CR energy losses.

Equation 6 encompasses the three modes of CR transport that we have implemented. The first term on the left represents advection, in which the CR fluid moves with the bulk velocity of the thermal gas. This term is solved explicitly in the Riemann solvers of ENZO. The next two terms describe CR streaming and diffusion respectively. These are approximations to CR motion relative to the gas and are therefore solved separately from the advection equation. The implementation of these transport methods is described in detail in sections 2.2 and 2.3.

In the streaming approximation, CRs move relative to the gas with a velocity given by

$$\mathbf{v}_s = -\text{sgn}(\mathbf{b} \cdot \nabla \varepsilon_c) f_s \mathbf{v}_A \quad (7)$$

Here,  $f_s$  is the constant streaming factor described in Ruszkowski et al. (2017). The Alfvén velocity,  $\mathbf{v}_A = \mathbf{B}/\sqrt{4\pi\rho}$  represents the transverse waves propagating along the magnetic field lines in a plasma. The function  $\text{sgn}$  returns the sign of the enclosed expression. In this limit, CRs also transfer momentum to the thermal gas through the heating term,  $H_c$ , where

$$H_c = |\mathbf{v}_A \cdot \nabla P_c|. \quad (8)$$

Although this term appears only in the streaming approximation, we follow the example of Wiener et al. (2017) and include it in some simulations with CR diffusion to isolate the underlying differences in the different transport mechanisms (see Table 1).

## 2.2. Cosmic Ray Streaming

Both CR streaming and diffusion are approximations to CRs scattering off of Alfvén waves. The difference lies in the source that is generating these waves. In the streaming approximation, CRs are assumed to drive the growth of Alfvén waves through the streaming instability (Kulsrud & Pearce (1969). This is often referred to as the "self-confinement" case (Zweibel 2017).

We isolate the streaming behavior from the general CR transport equation (Eqn. 6) using

$$\frac{\partial \varepsilon_c}{\partial t} - \nabla \cdot [\mathbf{v}_s (\varepsilon_c + P_c)] = 0. \quad (9)$$

At each simulation timestep, we calculate CR streaming by updating the value of the CR energy density in each cell. The evolution of the CR energy density in cell  $i$  is given by

$$\varepsilon_{c,i}^{n+1} = \varepsilon_{c,i}^n - \Delta t \sum_j -\text{sgn}(\mathbf{b}_{ij} \cdot \nabla \varepsilon_{c,ij}^n) \mathbf{v}_{A,ij} \cdot \mathbf{n}_{ij} (\Delta x_{ij})^{-1}, \quad (10)$$

where  $\varepsilon_{c,i}^n$  is the value of the CR energy density in cell  $i$  before streaming is applied.  $\Delta t$  is the timestep, and the terms  $\mathbf{b}_{ij}$  and  $\nabla \varepsilon_{c,ij}$  are the direction of the magnetic field and the gradient of CR energy density computed at cell face  $j$ .  $\mathbf{n}_{ij}$  describes the plane parallel to face  $j$ , and  $\Delta x_{ij}$  is the length of the cell's axis

that is perpendicular to face  $j$ . If the cells in the simulation are constructed as cubes, then  $\Delta x$  can be treated as a constant and moved out of the summation term.

The streaming time step is set by the bulk motion of the gas and the Alfvén velocity, so that  $t_{\text{stream}} < \frac{\Delta x}{v_g + f_s v_a}$ . We avoid instabilities near local extrema of CR energy density by employing the regularization described in [Sharma et al. \(2009\)](#) and [Ruszkowski et al. \(2017\)](#) where

$$\mathbf{F}_c = -(e_c + p_c) \mathbf{u}_A \tanh(h_c \hat{\mathbf{v}} \cdot \nabla e_c / e_c). \quad (11)$$

We follow the recommendation of [Ruszkowski et al. \(2017\)](#) and set the free regularization parameter,  $h_c$ , to 10 kpc.

### 2.3. Cosmic Ray Diffusion

In the "extrinsic turbulence" case, Alfvén waves are excited by turbulent motions in the thermal gas. Since the gyroradius of CRs around magnetic field lines is significantly smaller than the best-resolved cells in our simulation, CR transport in this regime is modeled as diffusion parallel to the direction of magnetic field lines. At each timestep, in addition to solving the conservation equations, ENZO computes CR diffusion according to

$$\frac{\partial \varepsilon_c}{\partial t} - \nabla \cdot [\kappa_\varepsilon \mathbf{b}(\mathbf{b} \cdot \nabla \varepsilon_c)] = 0. \quad (12)$$

With diffusion, the updated CR energy density in a grid cell,  $i$  follows the prescription

$$\varepsilon_{c,i}^{n+1} = \varepsilon_{c,i}^n + \Delta t \sum_j \kappa_\varepsilon (\mathbf{b}_{ij} \cdot \nabla \varepsilon_{c,ij}^n) \mathbf{b}_{ij} \cdot \mathbf{n}_{ij} (\Delta x_{ij})^{-1}, \quad (13)$$

where  $\Delta t$  is the diffusion timestep.

In the case of isotropic diffusion, Equation 13 becomes

$$\varepsilon_{c,i}^{n+1} = \varepsilon_{c,i}^n + \Delta t \sum_j \kappa_\varepsilon \nabla \varepsilon_{c,ij}^n \cdot \mathbf{n}_{ij} (\Delta x_{ij})^{-1}. \quad (14)$$

We employ an explicit diffusion scheme because we find that our simulation time step is not limited by the diffusion time step constraint of  $t_{\text{diff}} < \frac{1}{2N} \frac{\Delta x^2}{\kappa_\varepsilon}$ , where  $N$  is the dimensionality of our simulation. For a detailed discussion on numerically modeling semi-implicit anisotropic CR diffusion, see [Pakmor et al. \(2016a\)](#).

### 2.4. Limiting the Gradient

For some geometrical configurations, using a simple estimate of the CR energy gradient when calculating anisotropic diffusion violates the second law of thermodynamics and leads to an unphysical flow of CR energy from cells with lower energy density to cells with higher energy density. In more extreme cases, this leads to some cells developing unphysical (negative) values of CR energy. To combat this issue, we employ a limited gradient as described in [van Leer \(1977\)](#).

The simple gradient only considers the flux through a given cell face, so that

$$\nabla \varepsilon_c = \frac{\varepsilon_{c,i+1} - \varepsilon_{c,i}}{\Delta x_i} \quad (15)$$

where  $i$  and  $i+1$  are the indices of neighboring cells.

Where the simple gradient produces an unphysical flux, we estimate the limited CR energy density gradient on the interface ([Sharma & Hammett 2007](#); [Pakmor et al. 2016a](#)) to be

$$\nabla \varepsilon_c = \frac{4}{\sum_n (\nabla \varepsilon_{c,cr}^n)^{-1}}. \quad (16)$$

This approximation takes into account the component of the gradient that is parallel to the cell face,  $n$ .

## 3. NUMERICAL METHODS

We conduct our work using ENZO, an open source multi-physics MHD astrophysical simulation code that employs AMR to resolve areas of interest ([Collins et al. 2010](#); [Bryan et al. 2014](#)). At each time step, ENZO solves the Riemann conservation equations. We employ the local Lax-Friedrichs Riemann solver (LLF; [Kurganov & Tadmor 2000](#)) to compute the flux at cell interfaces and spatial reconstruction is performed with the piecewise linear method (PLM; [van Leer 1977](#)). Time stepping is carried out with the total variation diminishing (TVD) 2nd order Runge-Kutta (RK) scheme ([Shu & Osher 1988](#)). To avoid creating unphysical magnetic monopoles, we employ a hyperbolic divergence cleaning approach first described by [Dedner et al. \(2002\)](#). Interested readers should see [Wang et al. \(2008\)](#); [Wang & Abel \(2009\)](#) for detailed discussions and extensive testing of the MHD formulation in ENZO.

### 3.1. Stellar Feedback

Star formation in our simulations follows the prescription described in [Cen & Ostriker \(1992\)](#) with minor modifications. Stars particles are only formed in grids at the maximum level of refinement that meet predetermined density, mass, and minimum dynamical time thresholds:  $\rho_{\text{cell}} > \rho_{\text{thres}}$ ,  $M_{\text{cell}} > M_{\text{thres}}$ ,  $t_{\text{cool,cell}} < t_{\text{dyn,min}}$ . The exact values for  $\rho_{\text{thres}}$ ,  $M_{\text{thres}}$ ,  $t_{\text{dyn,min}}$  depend on the resolution of the simulation, because a very resolved cell may not be capable of holding sufficient mass to satisfy the formation criteria. In our simulations, we choose  $\rho_{\text{thres}} = 3.0 \times 10^{-26} \text{ g cm}^{-3}$ ,  $M_{\text{thres}} = 3.0 \times 10^5 M_\odot$ ,  $t_{\text{dyn,min}} = 10 \text{ Myr}$ . Additionally, the gas in the parent cell must be collapsing (determined by measuring negative velocity divergence) and Jeans unstable. If all conditions are met, the parent cell produces a star cluster particle with 10% mass efficiency so that the initial mass is given by  $M_{\text{SC}}^{\text{init}} = 0.1 \rho_g \Delta x^3$ .

Over the course of 120 Myr, 25% of that mass is ejected into the cell in which the star cluster particle resides, modeling the effects of Type II supernovae. We inject  $10^{51}$  ergs of energy for every  $42 M_\odot$ , so that a star cluster particle of  $M = 3.0 \times 10^5 M_\odot$  expels a total of  $E_{\text{tot}} = 5.4 \times 10^{54}$  ergs of energy. In our model, this total energy is comprised of thermal, magnetic, and CR energy so that  $E_{\text{th}} = f_{\text{th}} E_{\text{tot}}$ ,  $E_B = f_B E_{\text{tot}}$ , and  $E_{\text{cr}} = f_{\text{cr}} E_{\text{tot}}$ , where  $f_{\text{th}} + f_B + f_{\text{cr}} = 1$ . We adopt a conservative estimate of  $f_B = 0.01$ ,  $f_{\text{cr}} = 0.1$  ([Wefel 1987](#); [Ellison et al. 2010](#)) and assume 2% of the ejecta to be metals.

### 3.2. Chemistry and Cooling

In our simulations, we explicitly track all ion species of hydrogen. All other species are tracked together in a metallicity variable. We calculate cooling using the GRACKLE chemistry library ([Bryan et al. 2014](#); [Smith et al. 2017](#)) that is integrated with ENZO. It uses pre-computed tables of metal cooling rates as functions of the gas density and temperature generated by CLOUDY ([Ferland et al. 2013](#)). In addition, we consider uniform photoelectric heating of  $8.5 \times 10^{-26} \text{ ergs s}^{-1} \text{ cm}^{-3}$  without selfshielding ([Tasker & Bryan 2008](#)). In our idealized isolated disk setup, we do not consider the ultraviolet background radiation from distant quasars and galaxies.

### 3.3. Synthetic Observations

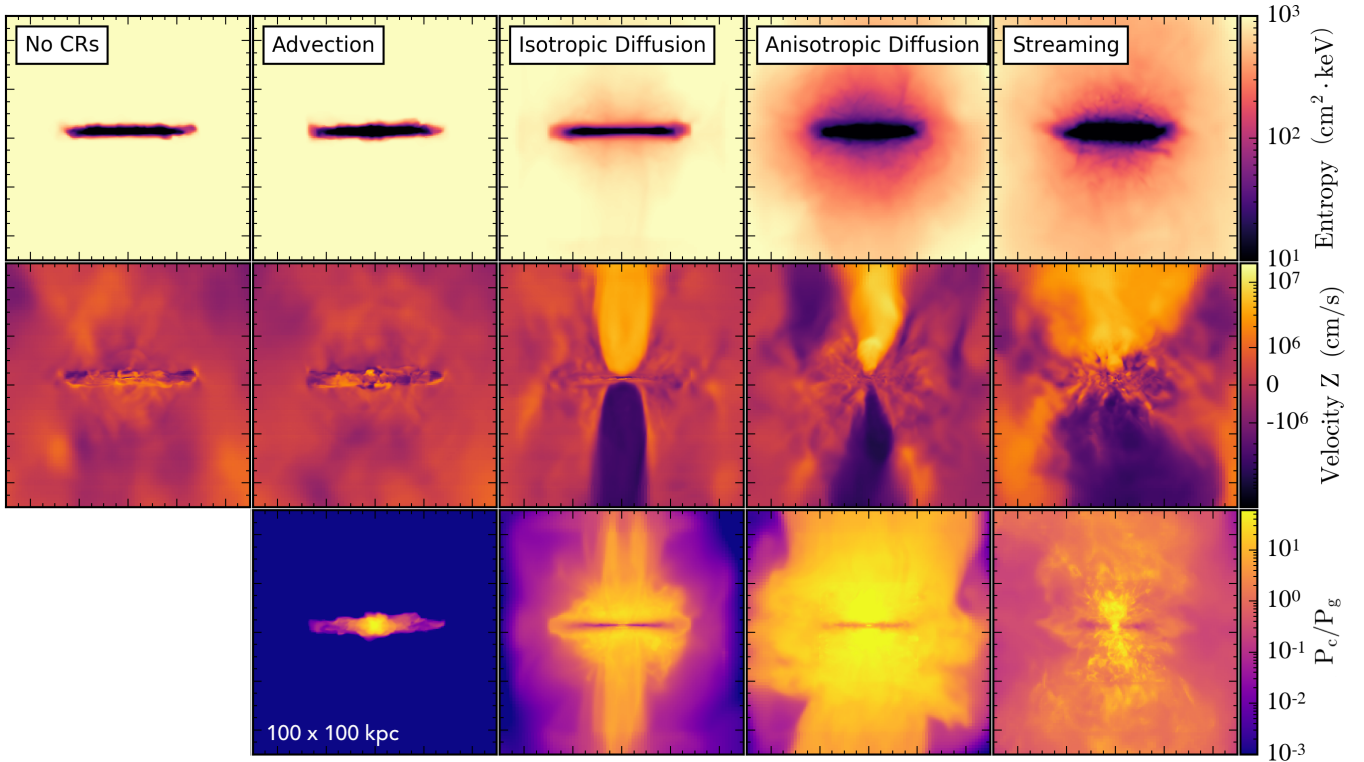


FIG. 1.— A comparison of the outflows between different galaxy models. Each row shows the edge-on, density-weighted projection of the gas entropy (top), z-component of the velocity (middle) and ratio of CR and thermal pressures (bottom). Each column holds a simulated galaxy with different CR treatment. From left to right, the columns show simulations with: no CRs, CR advection only, isotropic diffusion, anisotropic diffusion, and streaming. The snapshots were taken at  $t = 2$  Gyr. Only models with CR transport relative to the gas drive strong outflows by providing a non-thermal source of pressure to lift low-entropy gas out of the disk. The strength and morphology of the outflows is sensitive to the choice of CR transport.

We use *Trident* (Hummels et al. 2017), a python based tool integrated with yt (Turk et al. 2012) to construct ion densities and generate synthetic spectra from our simulated datasets. For ions that are not explicitly tracked by the simulation, we can determine their number densities,  $n_X$ , in post processing with

$$n_X = n_H Z \left( \frac{n_X}{n_H} \right)_{\odot}, \quad (17)$$

where  $n_H$  is the total hydrogen number density,  $Z$  is the metallicity (a value that is kept track of throughout the simulation), and  $(n_X/n_H)$  is the solar number abundance for any element that is not explicitly tracked.

*Trident* computes relative ion abundances in a simulation cell by considering both photoionization from an extragalactic UV background (Haardt & Madau 2012), and collisional ionization within the gas. The collisional ionization rate is determined by the cell's temperature, density, and metallicity, using an extensive set of lookup tables precalculated by CLOUDY, which assume ionization abundances as predicted by collisional ionization equilibrium (CIE). CIE holds even when CR pressure dominates over thermal pressure because the underlying assumption of our model is that the CR fluid is collisionless. Any deviations from CIE (which is more likely in the dense regions of the galactic disk than in the CGM) would likely increase of the ionization rate in low temperature gas (Oppenheimer & Schaye 2013).

We use this functionality in *Trident* to plot column densities of different ions as a function of impact parameter in Figure 9. We calculate the column densities by defining sight-lines

through the simulation box. The ion number density is then calculated in each length element,  $dl$ , along this projected ray. The column density along the line-of-sight is then given by the summation  $n_{\text{col}} = \sum dl \cdot n$ .

### 3.4. Initial Conditions

We simulate a suite of idealized isolated disk galaxies with initial conditions described by the AGORA collaboration (Kim et al. 2014). The fixed dark matter halo of mass  $M_{200} = 1.074 \times 10^{12} M_{\odot}$  follows the Navarro-Frenk-White (NFW; Navarro et al. 1997) profile and is situated in a hot ( $10^6$  K), stationary, uniform density box of  $(1.31 \text{ Mpc})^3$ . The concentration and spin parameters are respectively defined to be  $c = 10$ ,  $\lambda = 0.04$ . The gaseous disk has a total mass of  $M_d = 4.297 \times 10^{10} M_{\odot}$  and follows the analytic exponential profile

$$\rho(r, z) = \rho_0 e^{-r/r_d} e^{-|z|/z_d}$$

where  $r_d = 3.432$  kpc,  $z_d = 343.2$  pc, and  $\rho_0 = M_d f_{\text{gas}} / 4\pi r_d^2 z_d$ . We define  $f_{\text{gas}} = 0.2$  to be the gas mass fraction of the disk. The rest of the disk mass (80%) is contained in  $10^5$  stellar particles. The stellar bulge has a stellar mass of  $4.297 \times 10^9 M_{\odot}$  and follows the Hernquist density profile (Hernquist 1990).

We include an initial toroidal magnetic field of strength  $B_0 = 1 \mu\text{G}$  in the disk and a toroidal field of  $B_0 = 10^{-15}$  G in the halo. The strong initial field in the disk follows the example of Ruszkowski et al. (2017) to achieve sufficiently fast CR streaming velocities at early simulation times. The strength of the initial halo field lies in the accepted theoretical range

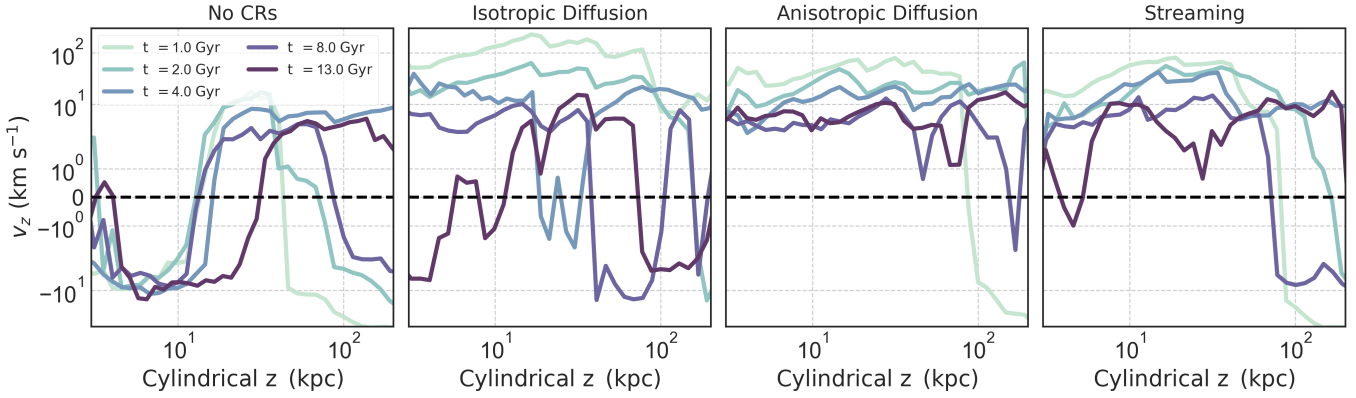


FIG. 2.— The time-evolution of the vertical velocity profile as a function of the height above the galactic disk for galaxy models NCR, ISOD, ANISD, and STREAM. Model NCR shows no signs of strong outflows. Model ISOD has the fastest outflow velocities but loses its galactic wind by  $t = 4$  Gyr. Models ANISD drive weaker yet steadier galactic winds. Model STREAM is the only model to develop inflows near the galactic disk while simultaneously hosting outflows at larger radii.

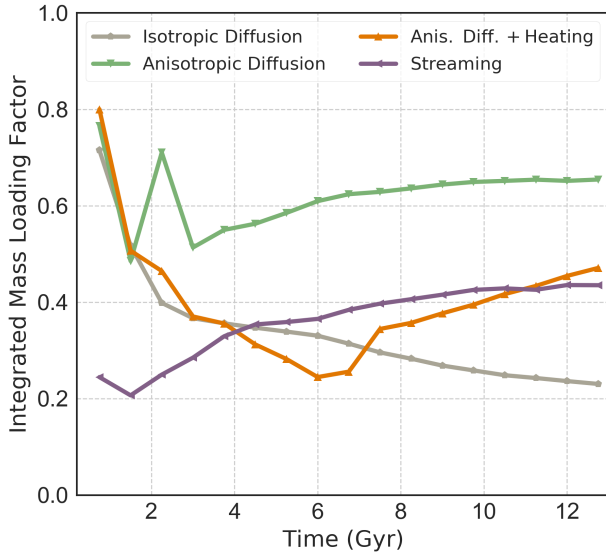


FIG. 3.— The time-evolution of the integrated mass loading factor (the total ejected gas mass / total mass in stars), measured at 150 kpc from the galactic center. At late times, models with anisotropic CR transport continue driving gas out of the galaxy, even when star formation is declining.

of primordial magnetic fields,  $10^{-20} - 10^{-9}$  G (Cheng et al. 1994; Durrer & Neronov 2013). To avoid numerical interpolation errors, galaxy models that include CR physics are initialized with an isotropic background CR energy density of  $0.1 \text{ erg/cm}^3$ . This background CR pressure is 15 orders of magnitude weaker than the initial conditions of the gas pressure and does not alter the thermal gas in any significant way. Because we’re interested in tracing the cycling process of metals, we set the initial metallicities of the disk and halo to be  $0.3Z_{\odot}$  and  $10^{-3}Z_{\odot}$  respectively.

### 3.5. Description of Simulation Suite

Our simulation suite is designed to isolate the effect of different implementations of CR transport. All of the galaxy models share the initial conditions described above. The fiducial models differ from each other only in their CR transport prescription and are described below:

- Model NCR does not include CR physics and serves as our control model.

- Model ADV only simulates CR advection with the bulk motion of the gas.
- Model ISOD assumes isotropic CR diffusion using the algorithm described in Salem & Bryan (2014) with a constant diffusion coefficient of  $\kappa_{\epsilon} = 3 \times 10^{28} \text{ cm}^2 \text{ s}^{-1}$ .
- Model ANISD assumes anisotropic CR diffusion along magnetic field lines with a constant diffusion coefficient of  $\kappa_{\epsilon} = 3 \times 10^{28} \text{ cm}^2 \text{ s}^{-1}$ .
- Model ANISDH builds on model ANISD with an added CR heating term,  $H_c$ .
- Model STREAM assumes CR streaming with a streaming factor of  $f_s = 4$  (Ruszkowski et al. 2017).

All of our fiducial models that include CR physics (in bold font in Table 1) inject 10% of their supernova ejecta in the form of CR energy. See Table 1 for a summary of the different models.

## 4. RESULTS

### 4.1. Outflows

The CGM in the isolated galaxy models is enriched solely by the outflows that expel gas from the disk. For this reason, we first turn our attention to analyzing the CR-driven winds and their dependence on the CR transport mechanism.

In broad strokes, a CR-driven wind begins when CRs move down their gradient, out of the midplane of the galaxy. CR pressure support then lifts low-entropy gas out of the galactic potential well, triggering outflows. Figure 1 displays the relationship between gas entropy (top row), the vertical component of the velocity of the galactic winds (middle row), and the ratio of CR to thermal pressures (bottom row) after 2 Gyr of evolution. From left to right, the columns show models with: No CR physics (NCR), CR advection (ADV) only, isotropic CR diffusion (ISOD), anisotropic CR diffusion (ANISD, and CR streaming (STREAM)).

Although models NCR and ADV experienced a brief period of weak gas expulsion, by  $t = 2$  Gyr these galaxies have lost all signs of outflows and show no signs of strong inflows. This is reinforced by the gas entropy profiles, which resemble the initial conditions. The main difference between models NCR and ADV at this time is near the midplane of the galaxy, where

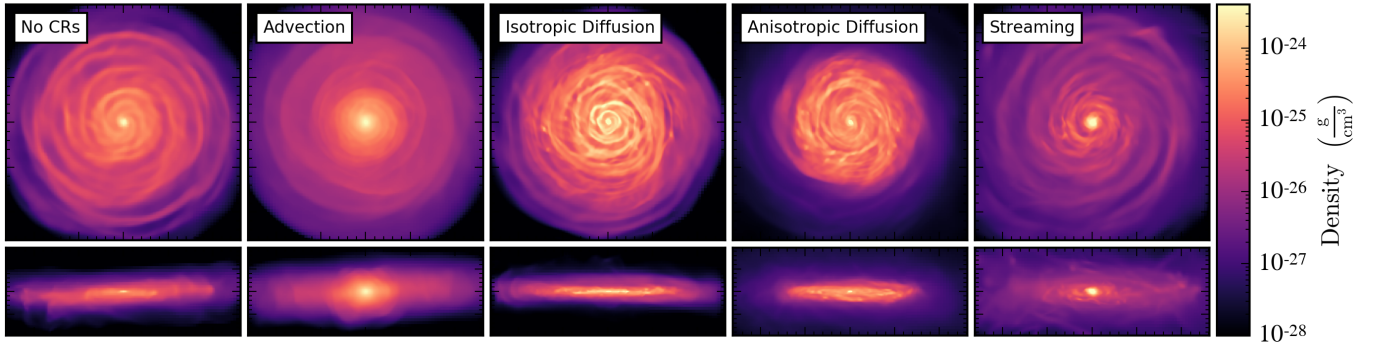


FIG. 4.— The face-on (top) and edge-on (bottom) density projections of the gas in our fiducial models after 13 Gyr of evolution. Although all galaxy models started from the same initial conditions, their morphologies depend on the CR transport mechanism. The control model, NCR, is a MW-type spiral galaxy. Models ADV and STREAM have extended gas profiles and thick disks. Model ANISD has lost much of its gas to outflows. The top and bottom rows show physical scales of  $52 \times 52$  kpc and  $20 \times 52$  kpc respectively.

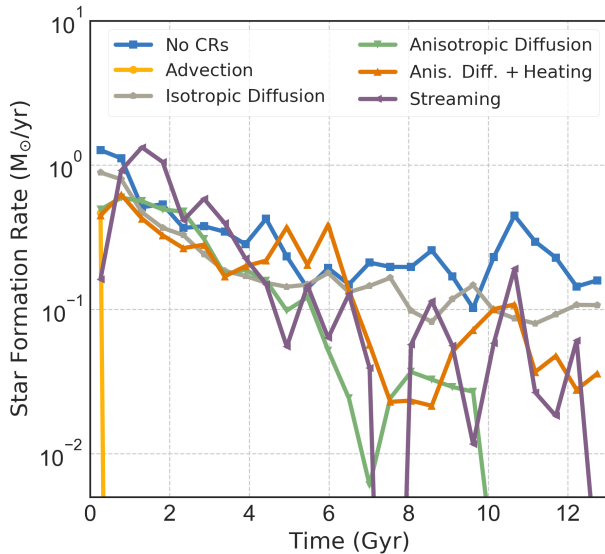


FIG. 5.— The star formation rate as a function of time for galaxy models with different CR transport prescriptions. Model ADV quenches after the first episode of star formation. The star formation in model ISOD consistently lies just below that of the control model NCR with no CRs. Model ANISD briefly matches the star formation in the control around  $t = 2.5$  Gyr, but is quenched soon after at around  $t = 10$  Gyr. Model STREAM has a variable star formation history with a period of roughly 2 Gyr.

the CR pressure of model ADV has created a thicker vertical disk profile. Confined to move solely through advection, the CRs in model ADV have no efficient mechanism for escaping the disk.

Models with CR transport relative to the gas (ISOD, ANISD, and STREAM) all drive strong outflows with velocities reaching  $10^2$  km/s, consistent with previous works (e.g. Salem et al. 2016; Pakmor et al. 2016b; Wiener et al. 2017).

Model ISOD drives relatively thin and uniform conical outflows. The gas entropy profile is relatively unaltered, reaching values near  $5 \times 10^2$  cm<sup>2</sup> keV near the midplane of the disk. CR pressure dominates over thermal pressure, tracing the shape of the outflows out to a cylindrical radius of 10 kpc. Outside of the active outflow region, the CR pressure is below one tenth of the gas pressure.

The outflows generated with anisotropic CR diffusion in model ANISD have a thinner radial profile and reach higher velocities compared to those driven by isotropic diffusion. For  $z > 20$  kpc outside of the midplane, there are signs of infalling

gas surrounding the outflow. The CR pressure dominates over thermal pressure for nearly all radii in the  $100 \times 100$  kpc projection. The gas entropy reaches values of  $50$  cm<sup>2</sup> keV just outside the disk, roughly an order of magnitude lower than that in model ISOD.

Compared to both of the diffusion models, the outflows generated by CR streaming start higher above the midplane of the disk and have a wider horizontal extent, reaching radii of nearly 40 kpc at a vertical height of 50 kpc. Near the galactic center, there are several filaments of inflowing gas. Compared to model ANISD, model STREAM has lower gas entropy immediately outside the disk and at larger radii, maintaining values around  $5 \times 10^2$  cm<sup>2</sup> keV at radii 50 kpc. Unlike either of the diffusion models, the distribution of the CR pressure ratio in model STREAM is patchy, ranging from 0.2 - 50 times that of the thermal pressure.

Figure 2 follows the time evolution of the density-weighted outflow velocity as a function of the height above the galactic disk, for models with different CR transport prescriptions. At early times, gas in our control model, NCR, is inflowing at all radii within 200 kpc of the galactic center. After 2 Gyr, weak ( $v_z = 10$  km/s) outflows develop at heights above 30 kpc. As we shall see in Figure 6, these weak outflows fail to enrich the CGM with metals. Instead, we turn our attention to models ISOD, ANISD, and STREAM, for which 10% of supernova feedback was injected as CR energy.

Model ISOD has the strongest outflows at  $t = 1$  Gyr, with radially-averaged velocities surpassing 100 km/s. By  $t = 4$  Gyr, these outflows weaken significantly, with average velocities hovering around 10 km/s. After 8 Gyr, notable inflows develop at radii above 30 kpc and persist for the rest of the simulation time.

This galactic wind is consistent with expectations of isotropic CR diffusion. The initial burst of supernova feedback in model ISOD creates a steep gradient of CR energy density. With isotropic diffusion, CRs drag gas out of the galaxy as they travel down their own gradient, uninhibited by the presence of magnetic fields. This process continues until the CR gradient flattens, slowing down the diffusion process. At later times, the star formation has decreased enough that the newly-injected CRs can no longer create a gradient steep enough to drive a strong wind. As the CRs in the CGM continue to stream away from the galaxy, they can't provide enough pressure support to the gas they expelled and it begins to collapse back down on to the galaxy.

Model ANISD retains consistent outflow velocities within

50 kpc of the disk throughout its evolution. Beyond 50 kpc, the winds are sensitive to the star formation history. For example, the double-valley feature at  $t = 8$  Gyr traces the suppressed star formation at  $t = 7$  Gyr (see Figure 5).

The steady nature of the galactic outflows in model ANISD is fueled by anisotropic CR diffusion. In this approximation, the velocity with which CRs can escape the disk is regulated by the complex geometry of magnetic field lines. Therefore, the galaxy releases its built-up CR energy slowly over time. Although the galaxy is quenched after  $t = 10$  Gyr, weak outflows in model ANISD persist out to  $t = 13$  Gyr.

Like in model ANISD, the key to sustained outflows in model STREAM is its anisotropic CR transport. Unlike any other fiducial run, model STREAM shows signs of inflow near the disk while simultaneously hosting outflows at larger radii.

The integrated mass loading factor (IMLF), defined as the ratio of the total injected gas mass over the total stellar mass, quantifies the expelled gas content. Figure 3 shows the evolution of the IMLF in models ISOD, ANISD, ANISDH, and STREAM. We exclude models NOCR and ADV, which didn't drive outflows, from this analysis.

For the first 1.5 Gyr, the IMLF is nearly indistinguishable between models ISOD, ANISD and ANISDH. The low IMLF at early times in model STREAM is most likely due to the later onset of the galactic wind as well as the wind's location above the galactic midplane.

At later times, the IMLF decreases in model ISOD, yet increases in the other three models. Model ANISD reaches the highest IMLF due to the accumulated reservoir of CR energy near the galactic disk that continues to drive outflows even after star formation has ceased. Models ANISDH and STREAM have weaker IMLFs than model ANISD due to higher star formation rates and losses in CR energy through the heating term.

#### 4.2. Star Formation and Morphology

The relationship between CR transport and a galaxy's star formation rate (SFR) can dramatically influence a galaxy's morphology. The outflows generated by different CR transport prescriptions remove gas from the disk which would have otherwise been available for star formation. In addition, the presence of strong CR pressure in the disk can prevent star formation by stabilizing the thermal gas against collapse. In this section, we contrast the morphologies of our fiducial galaxy models after evolving the simulations for 13 Gyr. Because a galaxy's morphology is so intricately tied to its star formation history, we describe Figures 4 and 5 simultaneously.

Figure 4 displays the density-weighted face-on and edge-on projections of the gas density in our fiducial galaxy models after 13 Gyr of evolution. In the left panel, model NCR serves as the benchmark example of a MW-type disk galaxy. This galaxy has a clear spiral structure, with the disk extending to a radius of roughly 25 kpc and a vertical height of roughly 3 kpc. The star formation rate of model NCR begins with one solar mass per year and slowly decreases over time, hovering around a few tenths of a solar mass at later times. With a modest star formation history and no galactic winds, model NCR retains much of its gas in its disk, with average density values around  $3 \times 10^{-25}$  g/cm<sup>3</sup>.

Although model ADV has had a similar outflow history as NCR, its star formation history has dramatically altered its morphology. Model ADV quenched only 200 Myr after its initial burst of star formation (see Figure 5). Confined to advection-only transport, the CRs in this galaxy are trapped

inside the galactic disk. After the first episode of star formation induces CR feedback, CR pressure dominates over gas pressure (see the bottom-left panel of Figure 1 and the discussion in §4.1). This additional pressure stabilizes the gas against collapse, halting future star formation. Without galactic outflows to carry CRs out of the disk and without any new stars to create supernovae that could potentially drive outflows, this galaxy will remain quenched. Although model ADV has a substantial reservoir of gas in its disk, CR pressure expands its vertical profile keeping the gas at lower average densities.

The star formation history of model ISOD most closely follows that of model NCR. Episodes of star formation that expel CRs into the disk keep the SFR of model ISOD consistently below that of the control. However, because isotropic diffusion is efficient at removing CRs from the galactic disk, star formation is only weakly suppressed in this galaxy. The morphology of model ISOD is qualitatively similar to that of model NCR out to a cylindrical radius of 15 kpc. Having expelled much of its ISM through outflows, model ISOD has a shorter radial and vertical extent to its gas.

Anisotropic CR transport in model ANISD retains CR pressure in the disk, which suppresses star formation at early times. As galactic outflows develop, the CR pressure is lifted out of the disk, allowing for star formation to resume. After roughly 2 Gyr of evolution the star formation in model ANISD briefly matches that of the control model. The injected CR pressure following this star formation episode decreases future star formation, ultimately quenching the galaxy after 10 Gyr. CR heating in model ANISDH relieves some of the CR pressure in the disk, leading to a higher star formation rate than that in model ANISD. Although at the time of the snapshot in Figure 4 model ANISD has been quenched for 3 Gyr, this galaxy model retains some spiral structure and high gas densities within a 15 kpc radius of its center. The lingering CR pressure from past star formation creates an extended low-density gas profile around the disk.

Both models ANISD and STREAM have extended, thick gaseous profiles that are most apparent in the edge-on view. Model ANISD has a bimodal distribution of gas, with a core around  $2 \times 10^{25}$  g/cm<sup>3</sup> extending to 15 kpc, surrounded by a less dense gaseous halo extending to 25 kpc. Although some spiral structure is present, it is significantly less pronounced than in model ISOD. Model STREAM has relatively low gas density in the disk with a spiral arm structure that is thinner than that of models NCR or ISOD.

Because of the toroidal geometry of the initial magnetic field, the CRs in model STREAM suppress star formation for the first 500 Myr. Once the magnetic field develops a sufficiently strong vertical component, the CRs escape the disk, dragging thermal gas along with them. The outflows relieve the ISM of the CR pressure, allowing star formation to resume. Filaments of inflowing gas near the midplane of the disk (see Figure 1) supply the additional gas necessary for extended episodes of star formation. Compared to the other galaxy models, model STREAM has the lowest gas densities and the most extended vertical and radial disk profile.

#### 4.3. The Simulated Circumgalactic Medium

We now turn our attention to the different ionization structures within the CGM of the simulated galaxy models. Our control model, NCR, has limited amounts of metals outside of the galactic disk. This is an unrealistic result and we will not dwell on its implications here. Our goal is to isolate the



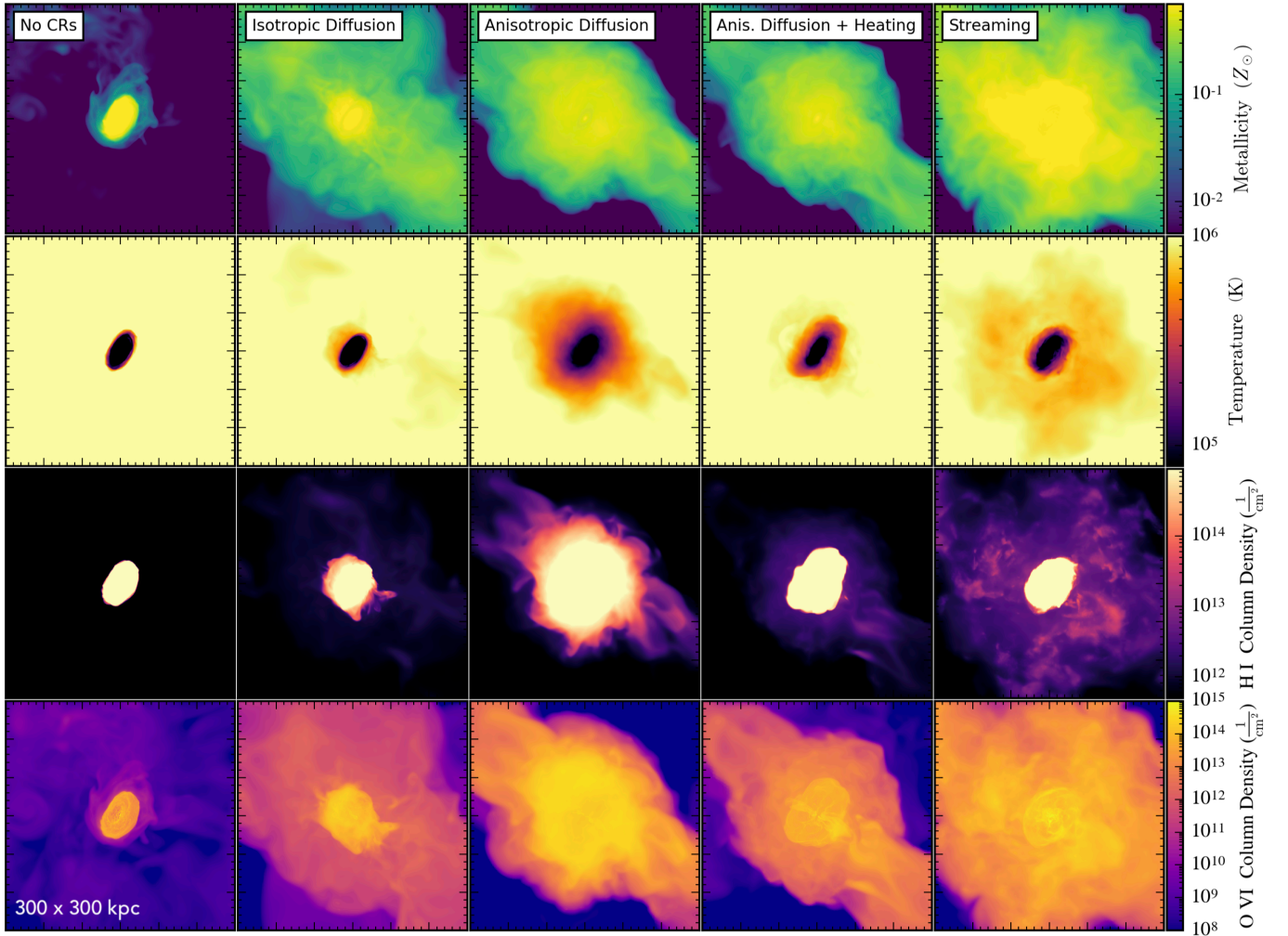


FIG. 6.— A comparison of the state of the CGM between the fiducial galaxy models after 13 Gyr of evolution. The top two rows show the density-weighted metallicity and temperature and the bottom two rows show the unweighted column densities of H I and O VI. Our control model NCR drove weak outflows, so the state of its CGM is relatively unaltered from the initial conditions. Model ISOD has a spatially uniform distribution of warm, metal-rich, gas in its CGM. The galaxy model ANISD is surrounded by a reservoir of cool gas, traced by H I. The temperature and ionization structure of model ANISDH follows the morphology of that in model ANISD although the effect of CR pressure is weakened through losses due to CR heating. Galaxy model STREAM has a patchy, multiphase distribution of different temperature gas, traced by its H I and O VI column densities. The projection is generated from a 300 kpc cube.

effects of CR transport on the CGM’s temperature and ionization structure, and so the following figures and discussions will focus on models ISOD, ANISD, and STREAM. Where relevant, we discuss model ANISDH, which includes the heating term  $H_c$ , that is present in the CR streaming prescription. Although the heating term is an unphysical addition to CR diffusion, its presence helps isolate which aspect of the CR streaming or diffusion mechanism is responsible for observed differences in temperature and ionization states (Wiener et al. 2017).

Figure 6 shows the density-weighted projections of gas metallicity and temperature and the unweighted projections of H I and O VI column densities after 13 Gyr of evolution. Each column holds a different mode of CR transport. Starting from the left, the columns show results for galaxy models NCR, ISOD, ANISD, ANISDH, and STREAM.

The outflows in models with CR diffusion or streaming have populated their CGM with metals from the disk out to radii surpassing 200 kpc. Model ISOD has a relatively uniform distribution of metallicity in its CGM, with a density-weighted average value around  $0.2 Z_\odot$ . Similarly, its temper-

ature, H I and O VI column densities are also spatially uniform. CR pressure support creates a cooler temperature profile (roughly  $3 \times 10^5$  K) compared to the control. The cooler temperatures result in stronger column densities of H I and O VI compared to model NCR.

Anisotropic diffusion in model ANISD produces a steep temperature and H I column density gradient. The temperature of the gas is coolest near the disk, where CR pressure is strongest, and decreases radially outwards. The H I column density follows the shape of the temperature profile, extending out to where the density-weighted temperature is  $10^6$  K. The O VI column density is sensitive to metallicity, so the column density profile traces the radial extent of the outflows. Compared to the other fiducial runs, model ANISD has the strongest column densities of H I and O VI. We point out that although this model has been quenched for 3 Gyr, the gradual release of CR pressure results in the accumulation of cold gas just outside the disk.

The metallicity distribution of model ANISDH is qualitatively similar to that of model ANISD. However, the added heating term dramatically decreases the impact of CR pres-

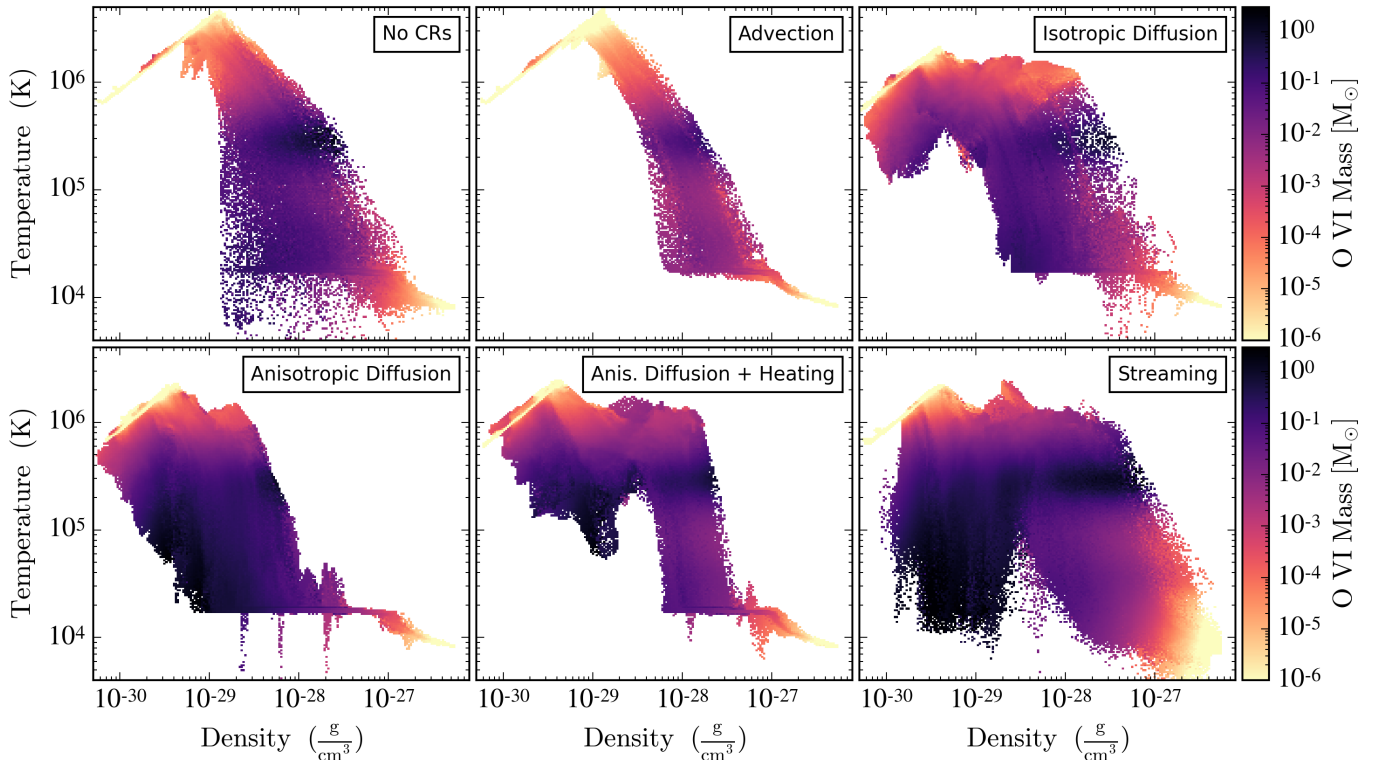


FIG. 7.— The 2D histograms of temperature as a function of density for the six different galaxy models after 13 Gyr of evolution. The color in the plot shows the mass of O VI in each bin. Model ISOD has more diffuse gas at larger radii. Model STREAM creates a more dramatic multiphase medium, with a larger range of possible densities for each temperature. Model STREAM supports an abundance of O VI at both warm and cool temperatures.

sure, resulting in warmer temperatures and weaker column densities of H I and O VI than those in model ANISD.

The outflows in model STREAM reach larger radii than those in model ANISD. The temperature profile is dominated by clumps of cool and warm gas extending out to radii of 150 kpc. Model STREAM has a patchy distribution of both H I and O VI column densities, with both coexisting in relative abundance at radii above 100 kpc from the galactic center.

#### 4.4. Temperature Distribution

To better understand the CGM structure, we analyze the abundance of O VI as a function of temperature and density in Figure 7. Since we are primarily interested with the gas in the CGM, we exclude data points contained within a cylindrical radius of 25 kpc and a vertical height of 3 kpc of the galactic center.

The CGM of models NCR and ADV has low masses of O VI and scarce amounts of low-density gas compared to the other models. Since low density values trace large radii in the CGM, the artificially high density floors are due to the lack of outflows. Suppressed star formation in model ADV is responsible for the low metallicities in its disk that ultimately result in low masses of O VI.

Models with additional CR transport drive strong outflows that enrich the CGM with metals (see Figure 6). This enrichment creates higher column densities of O VI at large radii. However, the different prescriptions for CR transport result in varied phase structures within the CGM.

One such difference is the shape of the temperature-density phase diagram. Models with weak CR pressure support (models ISOD and ANISDH) have less cool gas at low densities than models ANISD and STREAM. The strong CR pressure support

in models ANISD and STREAM supports a wide range of temperatures at each density. This feature is most pronounced at low densities in model STREAM.

CR transport also affects the abundance of O VI and the temperature of the gas that produces it. Both models STREAM and ANISD predict an a reservoir of O VI ionized with the help of CR pressure support in low-density gas. However, only model STREAM predicts an abundance of O VI photoionized with gas temperatures around  $3 \times 10^5$  K, consistent with predictions in McQuinn & Werk (2017).

Figure 8 shows the total enclosed mass as a function of spherical radius for six different galaxy models. The colors of the bars denote the fractional distribution of the gas temperature at different radial shells. We consider three temperature bins of gas: cold gas ( $T < 10^5$  K) in dark purple, warm gas ( $10^5$  K  $< T < 10^6$  K) in medium purple, and hot gas ( $T > 10^6$  K) in light purple. The colored gas fraction is not cumulative since the cold mass contribution from the disk would dominate the distribution in some cases.

Having driven weak outflows, model NCR has trace amounts of cold or warm gas outside of the disk. In contrast, although model ADV had similarly weak winds, the presence of CR pressure keeps the gas immediately around the disk below  $10^6$  K. The influence of CR pressure drops abruptly after a radius of 50 kpc. Because the CR pressure in the disk for this model stopped star formation almost immediately, model ADV has more gas available both inside and outside the disk of this model.

Models in which CRs can move relative to the gas (via diffusion or streaming) have an altered temperature structure in their CGM. Model ISOD is dominated by warm gas out to

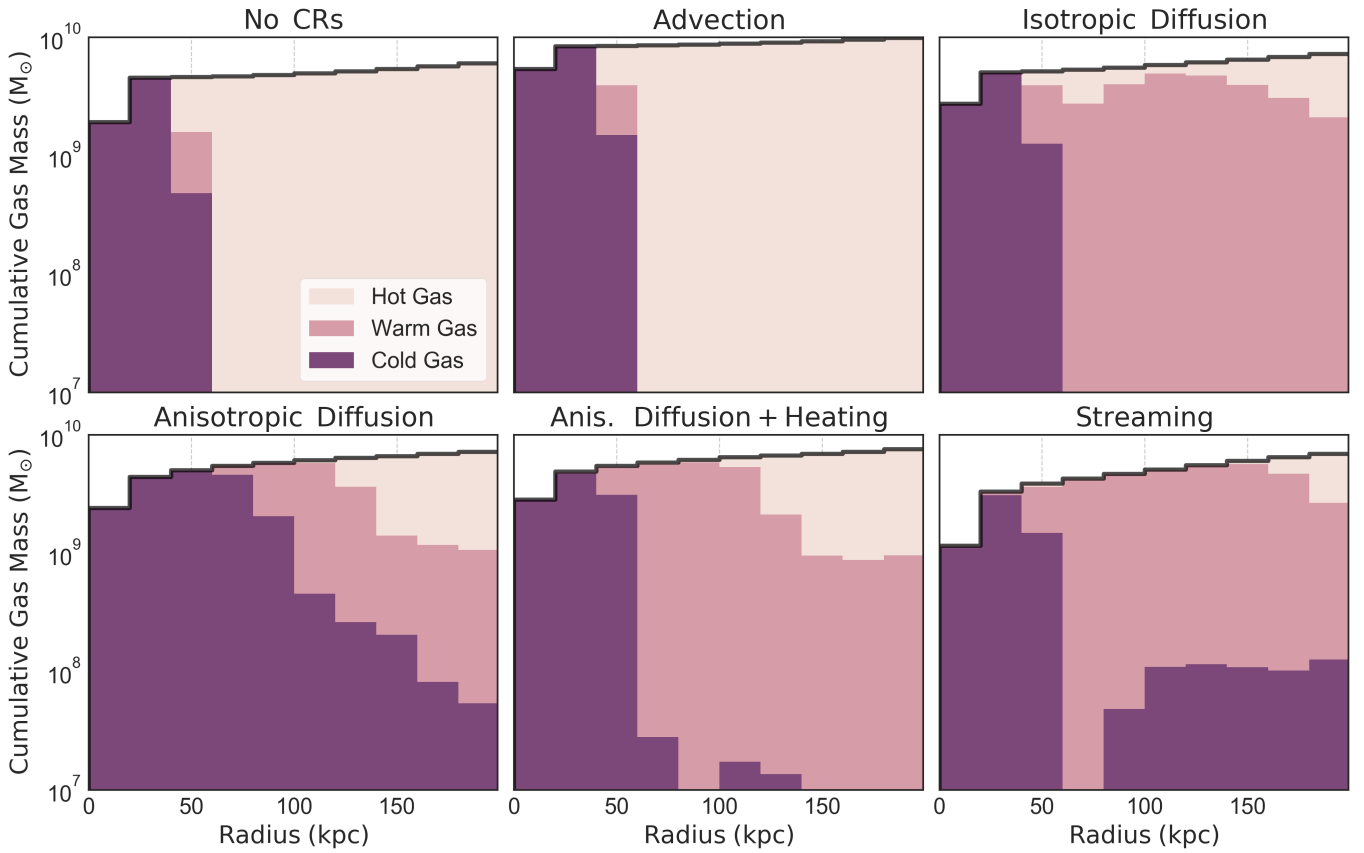


FIG. 8.— The black line follows total enclosed mass as a function of spherical radius for six different galaxy models. The colors of the bars denote the fractional distribution of the gas temperature at different radial shells. We consider three temperature bins of gas: cold gas ( $T < 10^5 K$ ) in dark purple, warm gas ( $10^5 K < T < 10^6 K$ ) in medium purple, and hot gas ( $T > 10^6 K$ ) in light purple. Only models with CR transport relative to the gas have a substantial amount of warm or cold gas in their CGM. Model ANISD has an abundance of cool gas near the galactic center that persists at large radii. Model STREAM has a truly multiphase medium with an abundance of cold and warm at radii of 200 kpc.

large radii. Since isotropic diffusion depends solely on the direction and magnitude of the CR energy density gradient, the CR pressure distribution is nearly uniform throughout the halo. Over time, with more stellar feedback releasing CRs into the disk, the CR pressure accumulates in the halo, providing pressure support to the thermal gas.

Models with anisotropic CR transport exhibit a multiphase temperature structure. Models ANISD and ANISDH are both dominated by cold gas near the disk. In both models, the cold gas extends out to radii of 125 kpc and the warm gas extends out to radii of 200 kpc.

Comparing this result with Figure 6, we see the cool gas, traced by H I column densities, decrease radially away from the center. The added heating term in model ANISDH converts some CR pressure, which is responsible for supporting the warm and cold gas, into heating the gas, consistent with results in Wiener et al. (2017). Even with the heating term, the distribution of warm gas in model ANISDH is still similar to that of ANISD.

Model STREAM shows signs of a true multiphase medium. This model has the lowest cumulative gas mass in its disk, likely due to its low gas densities and recent episodes of star formation (see Figure 5). Although warm gas dominates its CGM out to radii of 150 kpc, cold gas survives in abundance 200 kpc away from the galactic center. Using Figure 6, we see that the temperature structure in model STREAM does indeed result in a patchy, multiphase medium.

#### 4.5. Ionization Structure

Figure 9 holds the column densities of H I, Si IV, C III, and O VI as a function of the spherical radius from the center of the galaxy. Each scatter point in the plot represents one column density measurement at that radius. In each panel, we include points from both the fiducial model and its low-resolution counterpart. The solid black lines show the average column densities for the fiducial run while the dashed black lines show the average column densities for the lower resolution run with the same physics. For details on how the column densities were constructed, see §3.3.

To sufficiently sample our simulation space, we calculate the column densities at randomly-oriented sightlines passing through the CGM. To generate a sightline, we first select a random point on the sphere of radius  $r \in [10, 200]$  kpc from the galaxy center. We then chose a sightline by selecting a random angle in the plane tangent to the sphere at that point.

The control model, NCR, underpredicts the column densities of all four ions. This is both due to the lack of metals in its CGM and a deficit of cool gas.

Of the remaining models, model ISOD has the weakest column densities with a flat distribution across impact parameter. This picture is consistent with weak and spatially uniform CR pressure in the CGM. Model ANISD has stronger column densities with a wider spread at large radii. This is likely due to the uneven distribution of metallicity (see Figure 6). Model STREAM predicts column densities that are similar in strength

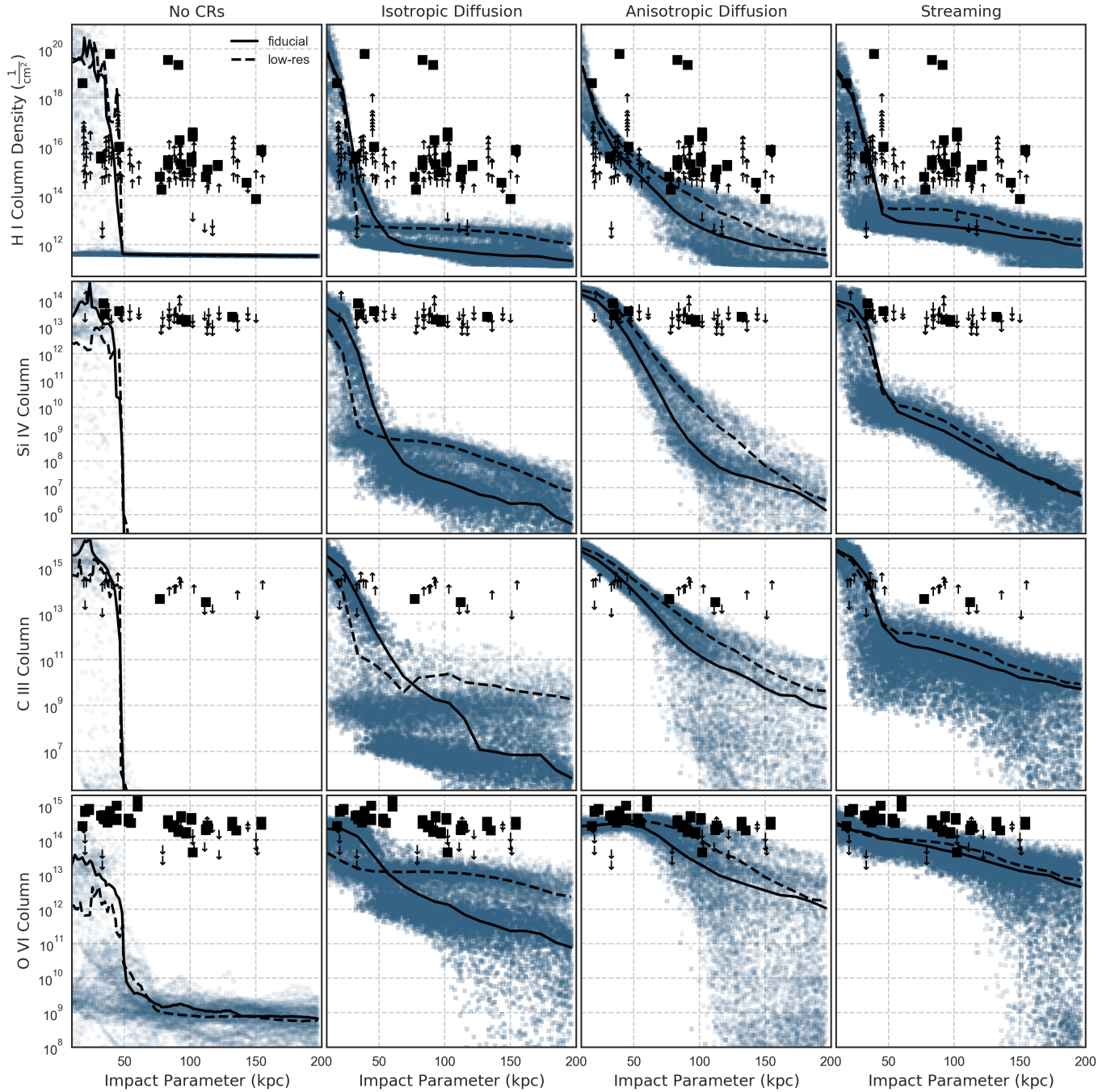


FIG. 9.— Column densities of H I, Si IV, C III, and O VI as a function of impact parameter after 13 Gyr of evolution. Each point on the graph shows a column density measurement using *Trident* from either the fiducial run described by the title, or its low-resolution counterpart. The overplotted black lines show the average column densities for the fiducial run (solid) and the low-resolution run containing the same physics (dashed). The black squares and arrows represent observed column densities and upper and lower limits from Werk et al. (2013). The control model underpredicts the observed column densities of all ions in this plot. Model ISOD has a flat column density profile with respect to impact parameter. The column densities in models ANISD and ANISDH decrease with radius. Model STREAM predicts the strongest column densities and is least sensitive to changes in resolution.

to model ANISD. However, the column density measurements in model STREAM are more tightly clustered around the average value, which is qualitatively similar to observations.

For all models, lower resolution predicts stronger column densities, possibly due to under-resolving the complicated structure of magnetic field lines. The column densities in model STREAM are the least sensitive to changes in resolution.

The column densities presented here are a qualitative example of the differences in ionization structure between different models of CR transport. In reality, the exact values of ion column densities would be influenced by the metallicity and inflows from the IGM. Therefore, in order to better match observations, we would need to simulate galaxies in a cosmological context.

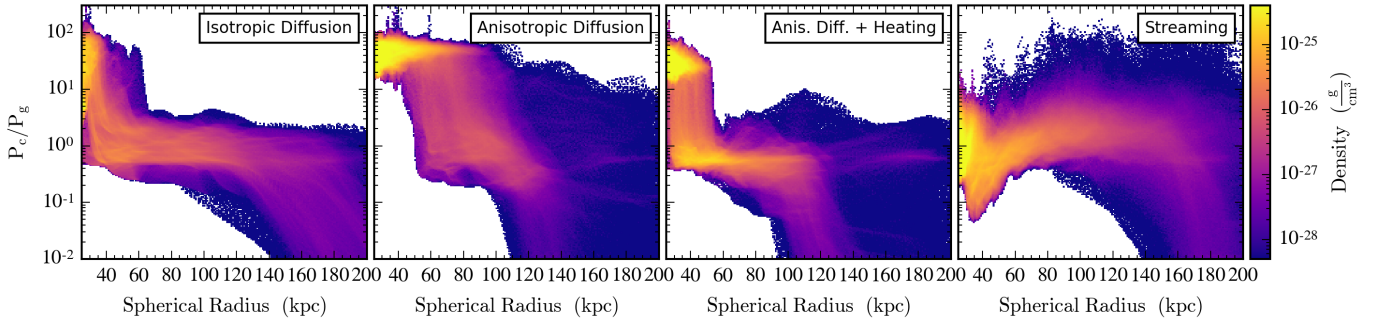


FIG. 10.— The unweighted ratio of CR pressure to gas pressure as a function of spherical radius, measured from the galactic center after 13 Gyr of evolution. The color of the bins shows the density of the gas. The disk has been removed from the dataset in order to focus on the CGM structure. Model ISOD has a relatively flat and unvarying profile of CR pressure in its CGM averaging around  $P_c/P_g \simeq 1$ . Models ANISD and ANISDH have a wide range of CR pressure in the CGM, with the highest values peaking near the disk center, at high gas densities. The CR pressure ratio in model STREAM peaks at larger radii, and at lower gas densities.

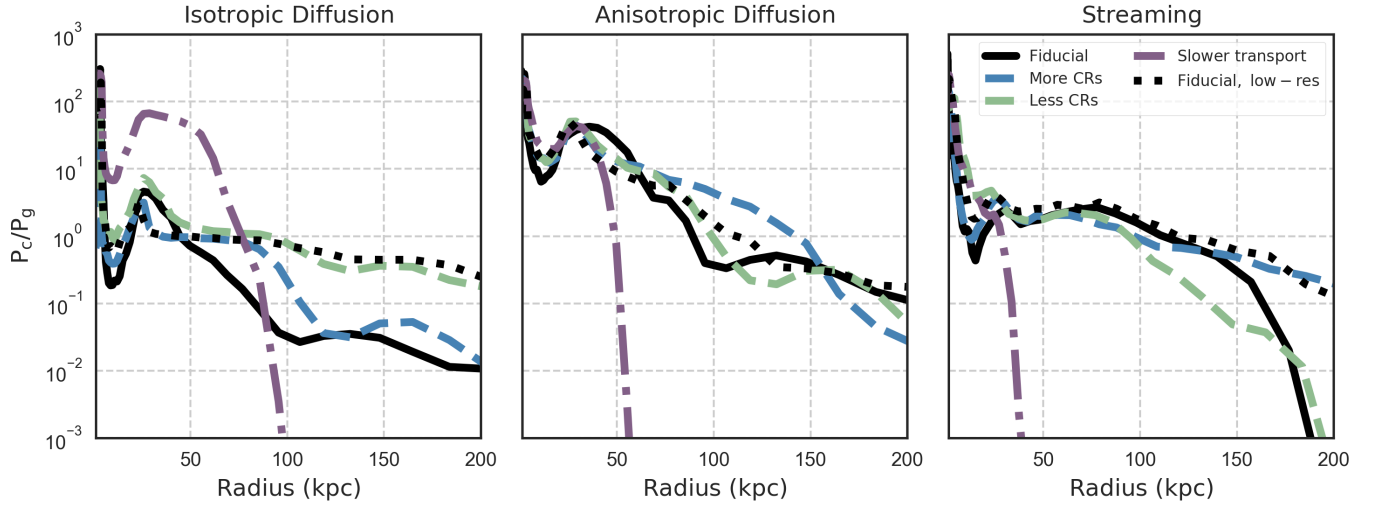


FIG. 11.— The density-weighted ratio of CR pressure to gas pressure as a function of spherical radius after 3 Gyr of evolution. The black solid line represents the values for the fiducial run of that CR transport method. Lines of different color and line style show variations from the fiducial run as described in the legend. The blue and green lines represent galaxy models with CR injection fractions of 0.3 and 0.01 respectively. The purple line represents a diffusion coefficient of  $\kappa_e = 10^{27} \text{cm}^2/\text{s}$  for galaxy models ISOD and ANISD and a streaming factor of  $f_s = 1.0$  for model STREAM. The red line represents a diffusion coefficient of  $\kappa_e = 10^{29} \text{cm}^2/\text{s}$  for model ANISD. For a description of the simulation parameters see Table 1. With this figure, we find that model ISOD is the most sensitive to parameter changes while model STREAM is the most robust.

#### 4.6. The Distribution of Cosmic Rays in the CGM

CR pressure in the CGM impacts the temperature and ionization structure of the gas. For this reason, we investigate the role of CR transport mechanisms in altering this CR pressure distribution.

In Figure 10 we explore the distribution of CR pressure as a function of spherical radius for models ISOD, ANISD, ANISDH and STREAM. The pixels in the phase plot are colored by the density of the gas. Like in Figure 7, we cut out the disk from our data sample.

Model ISOD has a flat and narrow profile of CR pressure as a function of radius, with the ratio  $P_c/P_g$  ranging between 0.5 and 5. At larger radii, the CR pressure ratio widens considerably, revealing regions where CR pressure is sparse.

Model ANISD has a much wider range of CR pressure ratios across all radii. Compared to isotropic diffusion, anisotropic diffusion creates CR pressure ratios that are nearly an order of magnitude higher across all radii. In this model, the CR pressure dominates over thermal pressure near the galactic disk and at high gas densities. The heating term in model ANISDH

lowers the CR pressure ratio at all radii. However, this model still retains the same qualitative shape of the CR pressure distribution that is present in model ANISD.

Although model STREAM also has a wide spread of CR to thermal gas pressure ratios, the distribution of that spread is qualitatively different from that in model ANISD. In this model, CR pressure in and near the disk is roughly 1.5 dex lower, spanning nearly 2 dex in strength. Unlike in model ANISD, the CR pressure is low near the galactic disk and dominates over thermal pressure at large radii (and low gas densities).

#### 4.7. Tuning the Knobs: The Impact of Choosing Parameters

Figure 11 shows the density-averaged ratio of CR to thermal pressure as a function of impact parameter, measured after 3 Gyr of evolution. The solid black line represents the low-resolution runs of our fiducial models. All other lines differ from this run only in the parameter specified in the label. Blue and green lines represent galaxy models in which su-

pernova feedback injected 1% and 30% of its energy as CRs, respectively. Purple lines represent slower CR transport velocities with either a diffusion coefficient of  $\kappa_\varepsilon = 10^{27} \text{cm}^2/\text{s}$  in models ISOD and ANISD or a streaming factor of  $f_s = 1.0$  in model STREAM. To better compare models with anisotropic diffusion to those with isotropic diffusion, we explore faster CR transport ( $\kappa_\varepsilon = 10^{29} \text{cm}^2/\text{s}$ ) in the middle panel, depicted by the red line. Finally, the black dotted line is the high-resolution fiducial run. For a summary of the parameters described above, see Table 1.

Varying the injected CR fraction does not correspond with a linear change in the ratio of CR to thermal pressure in the CGM. For example, increasing  $f_{CR}$  to 0.3 only marginally increases CR pressure in model ISOD. Counter-intuitively, increasing  $f_{CR}$  in models ANISD and STREAM actually decreases the CR pressure ratio in the CGM by suppressing star formation in the disk and thus preventing the injection of additional CRs. On the flip side, decreasing the injected CR fraction by a factor of 10 from the fiducial value does decrease the CR pressure in model ISOD by roughly an order of magnitude at radii above 100 kpc. However, this decrease in  $f_{CR}$  does not significantly alter the CR pressure ratio for models ANISD and STREAM.

The CR pressure distribution in all three models depends strongly on their transport velocities. Decreasing the diffusion coefficient by a factor of 10 limits the reach of outflows to 100 kpc in model ISOD and 60 kpc in model ANISD. Similarly, decreasing the streaming factor by four limits the reach of CR pressure to 40 kpc in 3 Gyr. In addition to limiting the radial extent of CR pressure, the decrease in transport velocity in model ISOD increases the CR pressure ratio by a factor of 10 at small radii. Increasing the transport velocity in model ANISD decreases the CR pressure within 75 kpc of the galactic center, but has no discernible effects at larger radii.

Doubling the resolution decreases the CR pressure ratio by roughly an order of magnitude for models ISOD and ANISD. In model STREAM, the CR pressure ratio of the higher resolution run only deviates from the fiducial run above 150 kpc.

Model ISOD is the most sensitive to changing parameters. In this approximation of CR transport, CRs can only move relative to the gas by diffusing down their own gradient. This motion is very sensitive to the injection fraction of CRs, which defines the strength of the CR gradient. Anisotropic diffusion is moderated by transport along magnetic field lines. The complicated geometry of the magnetic field lines slows anisotropic diffusion near the disk, making model ANISD less sensitive to the CR injection fraction and star formation history than model ISOD. The most robust model is STREAM, in which the CR transport depends on the CR gradient, magnetic field strength, and Alfvén wave velocity. The CR pressure ratio in all three models decreases with slower CR transport and increased resolution. Breaking this degeneracy will require additional parameter studies.

## 5. DISCUSSION

With our suite of isolated disk galaxy simulations, we have shown that the density, temperature, and ionization structures of the simulated CGM depend on the choice of CR transport mechanism. This discrepancy stems from the nature of the CR transport approximation and cannot be trivially remedied by altering constant parameters. In the following section, we will summarize the qualitative nature of each CR transport prescription and discuss potential improvements for future simulations.

The mere presence of CRs alongside thermal gas is not enough to drive galactic outflows. This point is demonstrated with model ADV, in which CRs are confined to propagate only through advection with the bulk motion of the thermal gas. These CRs provide pressure support to the gas within the disk but have no efficient mechanism through which to escape into the CGM. This added pressure stabilizes the gas against collapsing to form stars and thus quenches the galaxy almost immediately after the first episode of star formation. Although some CRs ultimately do escape the disk, there is no significant CR influence in the CGM after 13 Gyr of evolution.

CR transport *relative* to the thermal gas is necessary to drive galactic winds or to reproduce the observed column densities of ions in the CGM. As CRs move out of the disk, they provide pressure support which lifts low-entropy gas out of the gravitational potential well (see Figure 1). This additional CR pressure lowers the temperature and increases the ionization state of low ions, such as C III and Si IV, at large radii. However, the CGM structure depends on the distribution of CR pressure, which varies substantially between different CR transport models.

In the isotropic diffusion approximation, CRs move down their energy gradient with a velocity that is determined by both the strength of the gradient and the constant diffusion coefficient,  $\kappa_\varepsilon$ . The resulting galactic outflows and CGM are therefore sensitive to recent star formation, which injects CR energy into the ISM. The newly-ejected CRs propagate away from the galactic disk until the CR energy gradient is sufficiently flattened. Therefore, at late times, additional CR pressure injected by ongoing star formation can no longer drive strong outflows. Ultimately, the CR pressure in the CGM is unable to support the gas that it expelled at earlier times, triggering inflows. Varying the value of the constant diffusion coefficient alters the time scales on which the CR energy gradient flattens and the radial extent of CR energy, but not the qualitative shape of the CR distribution.

Although isotropic diffusion is a crude approximation to the true interactions between CRs and magnetic fields, it is a computationally frugal choice as it circumvents the need for fully MHD galaxy models. Simulations with isotropic CR diffusion have been successful at driving strong outflows and increasing the column densities of low ions in the CGM (Salem & Bryan 2014; Wiener et al. 2017). However, in our simulations, model ISOD was the least effective at producing a multiphase medium and the most sensitive to the choice of constant parameter values.

Anisotropic diffusion improves upon isotropic diffusion by approximating CR transport as a random walk down the CR energy density gradient, along the magnetic field. This transport around magnetic field lines modulates the velocity of CR transport. Near the disk, where the magnetic field lines are the most tangled, some CRs become trapped in their motion around magnetic field loops and make slow radial progress away from the disk. Simultaneously, CRs near magnetic field lines pointing out of the disk escape to larger radii. Therefore, anisotropic diffusion is capable of driving large-scale outflows while keeping a substantial presence of CR pressure near the disk. In this model, CR pressures are strongest near the galactic center and decrease rapidly at large radii. This CR pressure suppresses star formation in the disk and supports an abundance of cool gas in the halo. The strength and radial extent of the CR pressure depends on the constant diffusion coefficient, magnetic field topology, and the star formation history.

Increasing the diffusion coefficient in models with anisotropic diffusion counteracts the effect of tangled magnetic field lines near the galactic center. However, the resulting models are still not directly comparable to models with isotropic diffusion with a lower diffusion coefficient. The difference lies in the variable timing of the CR propagation. In anisotropic diffusion models, the CR pressure distributes itself preferentially along magnetic field lines, so the nominally constant diffusion coefficient becomes a function of the magnetic field geometry. There is no single ratio of diffusion coefficients that results in the same distribution of CR energy in both anisotropic and isotropic diffusion models.

CR streaming is the first-order approximation to CR transport. Streaming CRs move along magnetic field lines with a velocity that depends on the shape, *direction*, and *strength* of the magnetic field. This mode of transport creates a CR distribution in the CGM that supports a truly multiphase medium, with cold gas clumps surviving alongside a warm and hot medium. We find that compared to diffusion, streaming is less sensitive to changes in star formation history or the choice of constant parameter values.

A key component of the streaming approximation is the additional heating term, through which CRs give up their momentum to heat thermal gas. This transfer prevents simulations from overestimating CR pressure in the disk and halo. To discern the effect of the heating term from the streaming behavior, we simulated a galaxy with both anisotropic CR diffusion and CR heating (Wiener et al. 2017). Although the additional heating term increased temperatures and lowered the column densities of H I and O VI, the CR distribution in the CGM remained qualitatively the same. Therefore, we conclude that the key differences between the streaming and diffusion models lie in the transport approximations.

### 5.1. Limitations and Future Work

In this work, we explored the qualitative impact of the choice of CR transport on the simulated CGM. However, before simulations with CR physics can hold predictive power, several improvements must be made to constrain the details of this transport. We discuss these factors in greater detail below.

#### 5.1.1. Magnetic Fields

Magnetic fields are the media along which CRs propagate and are therefore crucially important for robust implementations of CR physics. The shape of the magnetic field dictates CR transport in the anisotropic diffusion and streaming approximations while the magnetic field strength sets the streaming velocity and the rate of heat transfer from CRs to the thermal gas. In addition, magnetic pressure is inversely proportional to the length scale of thermal instabilities in the CGM (Ji et al. 2017). Therefore, simulating CR transport and recreating the multiphase CGM requires a realistic treatment of magnetic fields.

Simulating the co-evolution of CRs and magnetic fields is complicated at early simulation times. The CRs streaming velocity depends on the magnetic field strength, yet primordial fields are believed to be no stronger than  $10^{-9}$  G (Cheng et al. 1994; Durrer & Neronov 2013). If newly-injected CRs cannot escape the galactic disk before the next round of star formation, the galaxy risks becoming immediately quenched.

One way to remedy this is to include magnetic supernova feedback, which can fuel the exponential magnetic field growth to observed values (Butsky et al. 2017). However, in

our attempts to simulate such a field, the small supernova injection sites were not sufficiently resolved to accurately capture CR transport. The overabundance of CR energy in the disk suppressed star formation, which in turn suppressed additional magnetic field injection. In these test simulations, the magnetic fields never reached observable strengths, and the streaming CRs never escaped the disk.

To circumvent this problem, we set the initial disk magnetic field to  $B_{0,d} = 1 \mu\text{G}$ , similar to that in Ruszkowski et al. (2017). This initial field is strong enough for CR streaming models to drive outflows that are comparable in their reach to outflows generated by the diffusion models with  $\kappa_\varepsilon = 10^{28} \text{cm}^2/\text{s}$ . The initial magnetic field in the CGM, which is the focus of this work, was set to  $B_{0,h} = 10^{-15}$  G. Therefore, the evolution of the of the magnetic field in the halo was driven by magnetized galactic winds and the turbulence they produced.

Improved implementation of the co-evolution of magnetic fields with streaming CRs will require detailed resolution and parameter studies which are outside of the scope of this work.

#### 5.1.2. Improved CR Physics

Our work makes several assumptions that are commonplace in current implementations of CR transport. One such approximation is that of a constant diffusion coefficient,  $\kappa_\varepsilon$ , which avoids calculating the momentum-weighted integral of the local CR energy density. The velocity of CR transport in the diffusion limit is therefore very sensitive to the choice of  $\kappa_\varepsilon$  (see Figure 11). Because the value of  $\kappa_\varepsilon$  is poorly constrained, simulations with the same model for CR transport can produce significantly varied results.

However, it is possible to improve upon the constant diffusion model without the computational expense of explicitly solving for the momentum-weighted value at every grid cell. For example, Farber et al. (2017) recently demonstrated that using a temperature-dependent, bimodal value for  $\kappa_\varepsilon$  alters galactic wind properties and spatial distribution of CRs.

The underlying assumption of our CR transport models is that CRs must propagate either in the diffusion limit or the streaming limit. Realistically, both modes of transport must be taking place. In a recent advancement, Jiang & Oh (2017) describe a new numerical scheme for CR transport that self-consistently handles both streaming and diffusion processes. This prescription is a promising new direction that may resolve the discrepancies between current implementations of CR transport presented in this work.

#### 5.1.3. Cosmological Context

The idealized experimental setup of isolated disk galaxies offers great control in isolating the effects of CR-driven galactic outflows on the structure of the CGM. However, this isolation comes at the expense of simulating a realistic CGM.

For example, the CGM in our simulations is populated almost entirely by CR-driven outflows. Neglecting inflows from the IGM leads to an unrealistically empty CGM, which is particularly apparent in our control model. The isolated disk galaxy model is an oversimplification of galactic evolution since most galaxies, including our own Milky Way, evolve in a group or cluster environment. Interactions with nearby galaxies and satellites can have a significant effect on the host galaxy's gas supply, which in turn affects its ability to form stars and drive outflows. These interactions can also strip gas directly from the CGM.

We focus solely on the CGM of Milky Way-type galaxies, in which purely thermal feedback is successful at reproducing

galactic disk properties. However, the differences between CR transport mechanisms presented above may change with galaxy mass. For example, [Jacob & Pfrommer \(2017\)](#) recently showed that the strength and mass-loading factor galactic outflows driven by isotropic CR diffusion depends on the host galaxy's mass. This mass-dependency is likely to be present for anisotropic diffusion and streaming transport prescriptions. However, the nature of that relationship may change for different transport mechanisms.

Future parameter studies using cosmological simulations will be necessary to develop a robust prescription of CR transport. We judge our CR transport models by the temperature and ionization structure of the simulated CGM. However, CR collisions in the CGM are expected to account for up to 10% of the diffuse, isotropic gamma ray background ([Feldmann et al. 2013](#)). Therefore, observations of the diffuse gamma ray emissions, such as those taken with the Fermi-LAT telescope can be used to constrain CR transport models ([Ackermann et al. 2012](#)).

## 6. SUMMARY

Simulations including CR feedback are more effective at driving galactic outflows and reproducing the observed ionization structure in the CGM than models with purely thermal feedback. However, models for simulating CR feedback and transport are poorly constrained.

In this work, we demonstrate that galactic outflows and CGM structure are sensitive to the invoked CR transport mechanism. We achieve this by simulating a suite of isolated MW-type disk galaxies with three commonly-used prescriptions for CR transport relative to thermal gas: isotropic diffusion, anisotropic diffusion, and streaming. For completeness, we also include advection-only models, in which CRs are constrained to move with the bulk motion of the gas, and control models without any CR physics. The results are summarized below.

- Models with CR transport relative to the thermal gas (streaming or diffusion) drive strong outflows. These outflows are generated by CR pressure support, which lifts thermal gas higher out of the gravitational potential well. Models with no CR feedback and those with CR advection do not launch strong galactic winds.
- Models with isotropic diffusion launch the fastest winds that last around 5 Gyr. Models with anisotropic CR diffusion and streaming drive steady winds that persist after 13 Gyr of evolution. Models with anisotropic diffusion continue to drive outflows even after the galaxy is quenched. Models with CR streaming support simultaneous inflows near the disk and outflows at larger radii.
- All models with CR feedback suppress star formation by supporting thermal gas against collapse. The degree to which star formation is suppressed depends on the CR pressure within the disk. Models with pure CR advection quenched after the first episode of star formation. The star formation in models with isotropic diffusion closely followed that of the control. Models with anisotropic diffusion suppressed star formation more efficiently, ultimately quenching after 10 Gyr. Models with CR streaming had a cyclical star formation history, supported by inflows from the CGM.

- CR pressure in the CGM supports gas with cooler temperatures. However, that temperature structure is sensitive to the CR transport model. The CGM of models with isotropic diffusion is primarily composed of warm gas that is spatially uniform. Models with anisotropic diffusion produce large quantities of cool ( $T < 10^5 K$ ) gas out to radii of 100 kpc that remain even after star formation is quenched. This is an interesting example of a quenched galaxy with a reservoir of cool gas in its CGM (e.g., [Gauthier et al. \(2010\)](#); [Thom et al. \(2012\)](#)). Models with CR streaming produce a patchy, multiphase gas distribution with cool gas existing alongside warm and hot gas at large radii.
- CR pressure creates a multiphase medium, allowing gas of a given temperature to span several orders of magnitude in density. At late times, models with isotropic diffusion show a relatively uniform CGM temperature, whereas anisotropic diffusion and streaming models retain varied temperature profiles. In anisotropic diffusion models, the influence of CRs is strongest near the galactic center and decreases with spherical radius. In CR streaming models, the multiphase temperature structure is patchy, with clumps of cool gas existing 200 kpc from the galactic center.
- Models with anisotropic diffusion and streaming generate higher column densities of H I, Si IV, C III, and O VI than models with isotropic diffusion. The column densities generated by models with CR streaming have less variation in predicted column densities as a function of impact parameter and are less sensitive to changes in resolution.
- The differences between our galaxy models stem from the varied distribution of CRs in the CGM. Compared to isotropic diffusion, anisotropic diffusion and CR streaming are more effective at retaining CR pressure near the galactic disk. Since the transport in isotropic diffusion depends only on the gradient of CR energy density, its CR pressure support in the CGM decreases at late simulation times.
- The distribution of CR pressure in the CGM is sensitive to runtime parameters such as the amount of CRs injected in supernova feedback, the velocity of CR transport, and the resolution. We find that models with isotropic CR diffusion are the most sensitive to changes in these parameters. This is because the velocity of CR transport in this approximation depend only on the CR energy gradient and the choice of constant diffusion coefficient. The CR pressure distribution in models with anisotropic diffusion are less sensitive in comparison. We conclude that models with streaming, in which CR transport depends on the shape, direction, and strength of the magnetic field lines, are the most robust.

We have demonstrated that CR feedback can drive strong galactic outflows and provide the necessary pressure support to reproduce the multiphase temperature and ionization structure of the CGM. However, because the state of the simulated CGM depends strongly on the invoked CR transport method, it is necessary to first develop a robust numerical CR transport model before simulations with CR feedback can hold predictive power.



## 7. ACKNOWLEDGMENTS

The authors would like to thank the anonymous referee for their insightful suggestions. They also thank Cameron Hummels, Julianne Dalcanton, Juliette Becker, Jessica Werk, Matt McQuinn, Željko Ivezić, Victoria Meadows, and Scott Anderson for their valuable comments on this manuscript. I.B. also thanks Daniel Sotolongo for many helpful conversations.

I.B. was supported by the National Science Foundation (NSF) Blue Waters Graduate Fellowship. This research is part of the Blue Waters sustained-petascale computing project, which is supported by the National Science Foundation (Grants No. OCI-0725070 and No. ACI-1238993) and the State of Illinois. Blue Waters is a joint effort of the University of Illinois at Urbana-Champaign and its National Center for Supercomputing Applications.

## REFERENCES

- Abadi, M. G., Navarro, J. F., Steinmetz, M., & Eke, V. R. 2003, *ApJ*, 597, 21
- Ackermann, M., Ajello, M., Atwood, W. B., et al. 2012, *ApJ*, 750, 3
- Ackermann, M., Ajello, M., Allafort, A., et al. 2013, *Science*, 339, 807
- Agertz, O., Kravtsov, A. V., Leitner, S. N., & Gnedin, N. Y. 2013, *ApJ*, 770, 25
- Binney, J. 1977, *ApJ*, 215, 483
- Booth, C. M., Agertz, O., Kravtsov, A. V., & Gnedin, N. Y. 2013, *ApJ*, 777, L16
- Bordoloi, R., Lilly, S. J., Knobel, C., et al. 2011, *ApJ*, 743, 10
- Boulares, A., & Cox, D. P. 1990, *ApJ*, 365, 544
- Brio, M., & Wu, C. C. 1988, *Journal of Computational Physics*, 75, 400
- Bryan, G. L., Norman, M. L., O’Shea, B. W., et al. 2014, *ApJS*, 211, 19
- Butsky, I., Zrake, J., Kim, J.-h., Yang, H.-I., & Abel, T. 2017, *ApJ*, 843, 113
- Cen, R., & Ostriker, J. P. 1992, *ApJ*, 399, L113
- Chen, H.-W., Helsby, J. E., Gauthier, J.-R., et al. 2010, *ApJ*, 714, 1521
- Cheng, B., Schramm, D. N., & Truran, J. W. 1994, *Phys. Rev. D*, 49, 5006
- Christensen, C. R., Brooks, A. M., Fisher, D. B., et al. 2014, *MNRAS*, 440, L51
- Collins, D. C., Xu, H., Norman, M. L., Li, H., & Li, S. 2010, *ApJS*, 186, 308
- Creasey, P., Theuns, T., & Bower, R. G. 2013, *MNRAS*, 429, 1922
- Davé, R., Oppenheimer, B. D., & Finlator, K. 2011, *MNRAS*, 415, 11
- Dedner, A., Kemm, F., Kröner, D., et al. 2002, *Journal of Computational Physics*, 175, 645
- Drury, L. O., & Falle, S. A. E. G. 1986, *MNRAS*, 223, 353
- Durrer, R., & Neronov, A. 2013, *A&A Rev.*, 21, 62
- Ellison, D. C., Patnaude, D. J., Slane, P., & Raymond, J. 2010, *ApJ*, 712, 287
- Enßlin, T. A., Pfrommer, C., Springel, V., & Jubelgas, M. 2007, *A&A*, 473, 41
- Farber, R., Ruszkowski, M., Yang, H.-Y. K., & Zweibel, E. G. 2017, *ArXiv e-prints*, arXiv:1707.04579
- Feldmann, R., Hooper, D., & Gnedin, N. Y. 2013, *ApJ*, 763, 21
- Ferland, G. J., Porter, R. L., van Hoof, P. A. M., et al. 2013, *Rev. Mexicana Astron. Astrofis.*, 49, 137
- Fielding, D., Quataert, E., McCourt, M., & Thompson, T. A. 2017, *MNRAS*, 466, 3810
- Gauthier, J.-R., Chen, H.-W., & Tinker, J. L. 2010, *ApJ*, 716, 1263
- Girichidis, P., Naab, T., Walch, S., et al. 2016, *ApJ*, 816, L19
- Governato, F., Zolotov, A., Pontzen, A., et al. 2012, *MNRAS*, 422, 1231
- Green, J. C., Froning, C. S., Osterman, S., et al. 2012, *ApJ*, 744, 60
- Gutcke, T. A., Stinson, G. S., Macciò, A. V., Wang, L., & Dutton, A. A. 2017, *MNRAS*, 464, 2796
- Haardt, F., & Madau, P. 2012, *ApJ*, 746, 125
- Hernquist, L. 1990, *ApJ*, 356, 359
- Hopkins, P. F., Quataert, E., & Murray, N. 2012, *MNRAS*, 421, 3522
- Hummels, C. B., & Bryan, G. L. 2012, *ApJ*, 749, 140
- Hummels, C. B., Bryan, G. L., Smith, B. D., & Turk, M. J. 2013, *MNRAS*, 430, 1548
- Hummels, C. B., Smith, B. D., & Silvia, D. W. 2017, *ApJ*, 847, 59
- Jacob, S., & Pfrommer, C. 2017, *MNRAS*, 467, 1478
- Ji, S., Oh, S. P., & McCourt, M. 2017, *ArXiv e-prints*, arXiv:1710.00822
- Jiang, Y.-F., & Oh, P. 2017, *ArXiv e-prints*, arXiv:1712.07117
- Joung, M. R., Mac Low, M.-M., & Bryan, G. L. 2009, *ApJ*, 704, 137
- Jubelgas, M., Springel, V., Enßlin, T., & Pfrommer, C. 2008, *A&A*, 481, 33
- Jun, B.-I., Clarke, D. A., & Norman, M. L. 1994, *ApJ*, 429, 748
- Kacprzak, G. G., Churchill, C. W., Ceverino, D., et al. 2010, *ApJ*, 711, 533
- Keller, B. W., Wadsley, J., & Couchman, H. M. P. 2015, *MNRAS*, 453, 3499
- , 2016, *MNRAS*, 463, 1431
- Kim, J.-h., Wise, J. H., Alvarez, M. A., & Abel, T. 2011, *ApJ*, 738, 54
- Kim, J.-h., Abel, T., Agertz, O., et al. 2014, *ApJS*, 210, 14
- Kulsrud, R., & Pearce, W. P. 1969, *ApJ*, 156, 445
- Kumar, R., & Eichler, D. 2014, *ApJ*, 785, 129
- Kurganov, A., & Tadmor, E. 2000, *Journal of Computational Physics*, 160, 241
- Marasco, A., Debattista, V. P., Fraternali, F., et al. 2015, *MNRAS*, 451, 4223
- McNamara, B. R., & Nulsen, P. E. J. 2007, *ARA&A*, 45, 117
- McQuinn, M., & Werk, J. K. 2017, *ArXiv e-prints*, arXiv:1703.03422
- Miniati, F., Jones, T. W., Kang, H., & Ryu, D. 2001, *ApJ*, 562, 233
- Murray, N., Ménard, B., & Thompson, T. A. 2011, *ApJ*, 735, 66
- Navarro, J. F., Frenk, C. S., & White, S. D. M. 1997, *ApJ*, 490, 493
- Nielsen, N. M., Churchill, C. W., & Kacprzak, G. G. 2013, *ApJ*, 776, 115
- Oppenheimer, B. D., & Davé, R. 2006, *MNRAS*, 373, 1265
- Oppenheimer, B. D., & Schaye, J. 2013, *MNRAS*, 434, 1043
- Oppenheimer, B. D., Segers, M., Schaye, J., Richings, A. J., & Crain, R. A. 2018, *MNRAS*, 474, 4740
- Pakmor, R., Pfrommer, C., Simpson, C. M., Kannan, R., & Springel, V. 2016a, *MNRAS*, 462, 2603
- Pakmor, R., Pfrommer, C., Simpson, C. M., & Springel, V. 2016b, *ApJ*, 824, L30
- Parrish, I. J., & Stone, J. M. 2005, *ApJ*, 633, 334
- Peebles, M. S., Werk, J. K., Tumlinson, J., et al. 2014, *ApJ*, 786, 54
- Pfrommer, C., Enßlin, T. A., & Springel, V. 2008, *MNRAS*, 385, 1211
- Pfrommer, C., Springel, V., Enßlin, T. A., & Jubelgas, M. 2006, *MNRAS*, 367, 113
- Pontzen, A., Roškar, R., Stinson, G. S., et al. 2013, *pynbody: Astrophysics Simulation Analysis for Python*, *astrophysics Source Code Library*, ascl:1305.002
- Prochaska, J. X., Weiner, B., Chen, H.-W., Mulchaey, J., & Cooksey, K. 2011, *ApJ*, 740, 91
- Ptuskín, V. S., Moskalenko, I. V., Jones, F. C., Strong, A. W., & Zirakashvili, V. N. 2006, *ApJ*, 642, 902
- Puchwein, E., & Springel, V. 2013, *MNRAS*, 428, 2966
- Rees, M. J., & Ostriker, J. P. 1977, *MNRAS*, 179, 541
- Rudie, G. C., Steidel, C. C., Trainor, R. F., et al. 2012, *ApJ*, 750, 67
- Ruszkowski, M., Yang, H.-Y. K., & Zweibel, E. 2017, *ApJ*, 834, 208
- Salem, M., & Bryan, G. L. 2014, *MNRAS*, 437, 3312
- Salem, M., Bryan, G. L., & Corlies, L. 2016, *MNRAS*, 456, 582
- Samui, S., Subramanian, K., & Srikanth, R. 2018, *MNRAS*, arXiv:1706.01890
- Schaye, J., Dalla Vecchia, C., Booth, C. M., et al. 2010, *MNRAS*, 402, 1536
- Sharma, M., & Nath, B. B. 2012, *ApJ*, 750, 55
- Sharma, P., Colella, P., & Martin, D. F. 2009, *ArXiv e-prints*, arXiv:0909.5426
- Sharma, P., & Hammett, G. W. 2007, *Journal of Computational Physics*, 227, 123
- Shu, C.-W., & Osher, S. 1988, *Journal of Computational Physics*, 77, 439
- Silk, J. 1977, *ApJ*, 211, 638
- Simpson, C. M., Pakmor, R., Marinacci, F., et al. 2016, *ApJ*, 827, L29
- Smith, B. D., Bryan, G. L., Glover, S. C. O., et al. 2017, *MNRAS*, 466, 2217
- Socrates, A., Davis, S. W., & Ramirez-Ruiz, E. 2008, *ApJ*, 687, 202
- Sod, G. A. 1978, *Journal of Computational Physics*, 27, 1
- Springel, V., & Hernquist, L. 2003, *MNRAS*, 339, 289
- Steidel, C. C., Erb, D. K., Shapley, A. E., et al. 2010, *ApJ*, 717, 289
- Stinson, G., Seth, A., Katz, N., et al. 2006, *MNRAS*, 373, 1074
- Stinson, G. S., Bovy, J., Rix, H.-W., et al. 2013, *MNRAS*, 436, 625
- Stocke, J. T., Keeney, B. A., Danforth, C. W., et al. 2013, *ApJ*, 763, 148
- Stone, J. M., & Norman, M. L. 1992, *ApJ*, 80, 753
- Strong, A. W., & Moskalenko, I. V. 1998, *ApJ*, 509, 212
- Suresh, J., Bird, S., Vogelsberger, M., et al. 2015, *MNRAS*, 448, 895
- Tabatabaei, F. S., Schinnerer, E., Murphy, E. J., et al. 2013, *A&A*, 552, A19
- Tasker, E. J., & Bryan, G. L. 2008, *ApJ*, 673, 810
- Thom, C., Tumlinson, J., Werk, J. K., et al. 2012, *ApJ*, 758, L41
- Tremmel, M., Karcher, M., Governato, F., et al. 2017, *MNRAS*, 470, 1121
- Tremonti, C. A., Heckman, T. M., Kauffmann, G., et al. 2004, *ApJ*, 613, 898
- Tumlinson, J., Werk, J. K., Thom, C., et al. 2011, *ApJ*, 733, 111
- Turk, M. J., Oishi, J. S., Abel, T., & Bryan, G. L. 2012, *ApJ*, 745, 154
- Turner, M. L., Schaye, J., Steidel, C. C., Rudie, G. C., & Strom, A. L. 2014, *MNRAS*, 445, 794
- Uhlig, M., Pfrommer, C., Sharma, M., et al. 2012, *MNRAS*, 423, 2374

van Leer, B. 1977, *Journal of Computational Physics*, 23, 276  
 Vazza, F., Brügggen, M., Gheller, C., & Brunetti, G. 2012, *MNRAS*, 421, 3375  
 Wang, P., & Abel, T. 2009, *ApJ*, 696, 96  
 Wang, P., Abel, T., & Zhang, W. 2008, *ApJS*, 176, 467  
 Wefel, J. P. 1987, *Origin and transport of high energy particles in the galaxy*, Tech. rep.  
 Werk, J. K., Prochaska, J. X., Thom, C., et al. 2013, *ApJS*, 204, 17  
 Werk, J. K., Prochaska, J. X., Tumlinson, J., et al. 2014, *ApJ*, 792, 8

Wiener, J., Pfrommer, C., & Peng Oh, S. 2017, *MNRAS*, 467, 906  
 Wise, J. H., Abel, T., Turk, M. J., Norman, M. L., & Smith, B. D. 2012, *MNRAS*, 427, 311  
 Zhang, H., Zaritsky, D., Zhu, G., Ménard, B., & Hogg, D. W. 2016, *ApJ*, 833, 276  
 Zweibel, E. G. 2017, *Physics of Plasmas*, 24, 055402

## APPENDIX

## TESTING THE NEWLY IMPLEMENTED CR PHYSICS

In §2, we described the implementation of CR physics into the Riemann solvers in Enzo. Here, we demonstrate the performance of our implemented CR advection, anisotropic diffusion, and streaming. For tests of the isotropic diffusion module, refer to [Salem & Bryan \(2014\)](#).

*Modified Sod Shock-tube*

The Sod shock-tube, first described in [Sod \(1978\)](#) is used to test the behavior of gas in the presence of a strong shocks in numerical simulations. Because the original Sod shock-tube doesn't include CRs, we use a modified version first described in [Pfrommer et al. \(2006\)](#). The initial conditions are described in Table 2.

In Figure 12 we test our implementation of the non-diffusive ( $\kappa_\varepsilon = 0.0$ ) two-fluid CR model and compare it to the existing implementation in the ZEUS hydro scheme in ENZO ([Salem & Bryan 2014](#)). From left to right, the panels show the density, velocity, and pressures of this shock-tube after  $t = 0.31$  code units of evolution. Where applicable, the analytic solution is depicted as a black dashed line. Compared to [Salem & Bryan \(2014\)](#), our implementation has a sharper velocity profile at  $x \simeq 250$  cm, but slightly under-predicts the density value around  $x = 400$  cm. Overall, the two implementations of CR advection agree well with each other and with the analytic solution.

TABLE 2  
INITIAL CONDITIONS FOR THE MODIFIED SOD SHOCK-TUBE

	$\rho$	$P_g$	$\varepsilon_c$	$v$
Left	1.0	$2/3 \times 10^5$	$4.0 \times 10^5$	0.0 <sup>a</sup>
Right	0.2	267.2	801.6	0.0

<sup>a</sup>The initial density, thermal pressure, CR energy density, and velocity for the modified Sod shocktube. The left and right regions of the shocktube are defined as ( $0 < x < 250$  cm) and ( $250 < x < 500$  cm) respectively.

TABLE 3  
MODIFIED BRIO-WU SHOCK-TUBE

	$\rho$	$P_g$	$\varepsilon_c$	$v_x$	$v_y$	$B_x$	$B_y$
Left	1.0	0.6	1.2	0.0	0.0	1.0	1.0 <sup>a</sup>
Right	0.125	0.06	0.12	0.0	0.0	1.0	-1.0

<sup>a</sup>The initial density, thermal pressure, CR energy density, velocity and magnetic field strengths for the modified Brio-Wu shocktube. The left and right regions of the shocktube are defined by ( $-0.5 < x < 0$ ) and ( $0 < x < 0.5$ ) respectively.

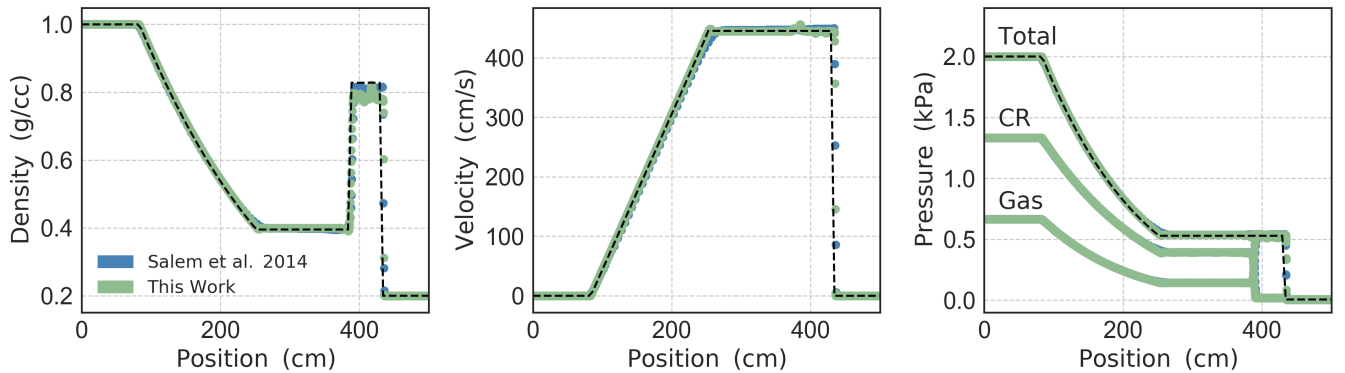


FIG. 12.— The density, velocity, and pressure (thermal, CR, and total pressures) as a function of position in a 1D simulation of the modified Sod shock-tube. CR pressure complements thermal pressure while the total pressure remained unchanged in the rarefaction wave.

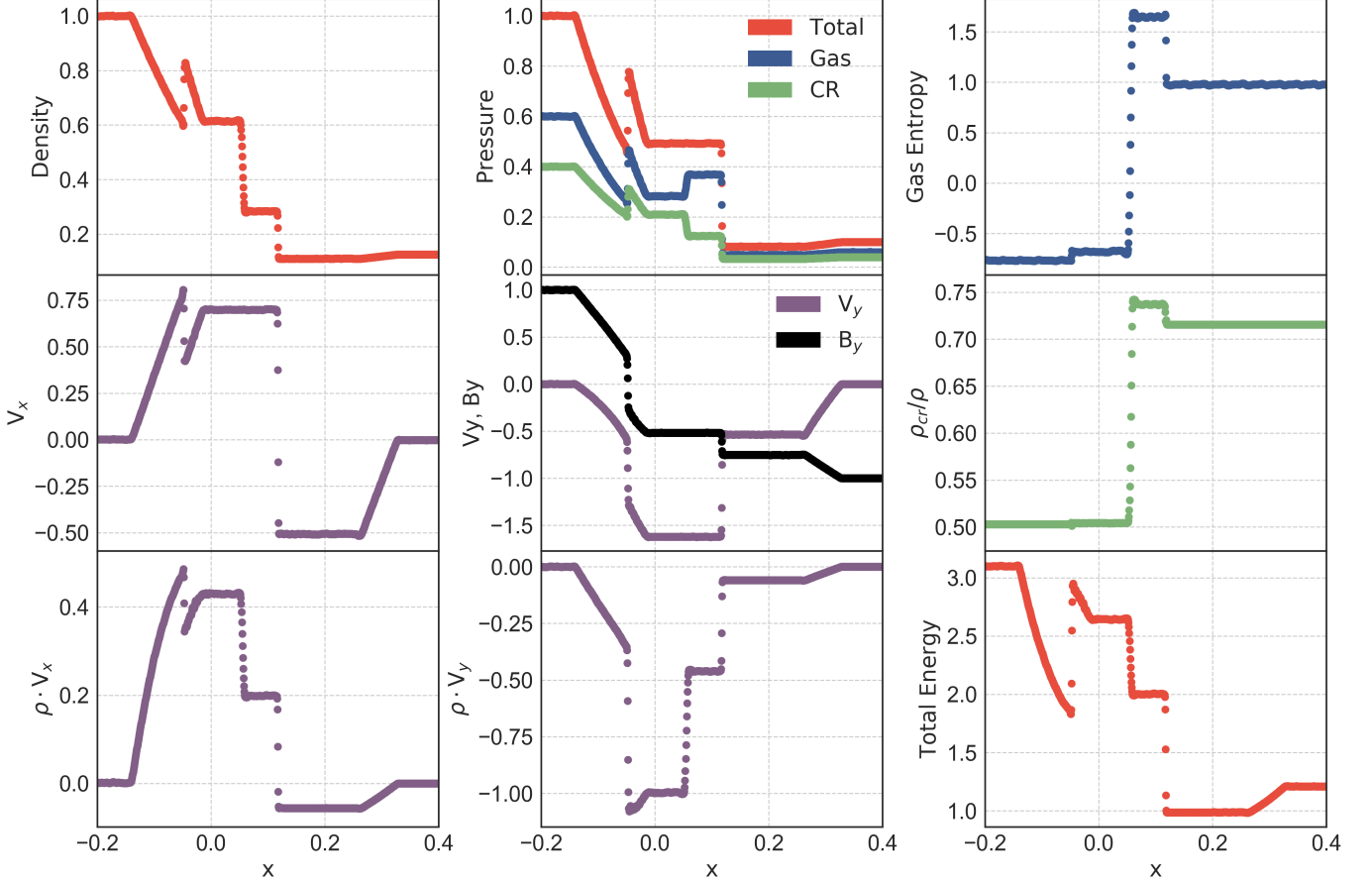


FIG. 13.— Various parameters of the modified Brio-Wu MHD shock-tube as a function of one dimensional position. **Top row:** density, CR, thermal, and total pressure, and thermal gas entropy. **Middle row:** x-component of the velocity, y-component of the velocity and magnetic field, ratio of CR density to thermal density. **Bottom row:** the density-weighted x and y components of the velocity, and the total energy. Thermal gas is influenced by the pressure of both CRs and magnetic field lines.

#### Brio Wu Shock-tube

The Brio-Wu shock-tube [Brio & Wu \(1988\)](#) tests the advection properties of gas interactions with magnetic fields in the presence of an extreme shock. In the modified Brio-Wu shock-tube, we include CR pressure and evolve the system for 0.2 code units. The initial conditions of the gas are described in [Table 3](#).

#### Anisotropic Diffusion

In the anisotropic diffusion approximation, CRs propagate down their gradient, along magnetic field lines. In [Figure 14](#), we test our implementation with the anisotropic ring problem initially described by [Parrish & Stone \(2005\)](#); [Sharma & Hammett \(2007\)](#) and explored in detail in [Pakmor et al. \(2016a\)](#). The experiment uses a uniform density box in with no gas (or a gas that is fixed in space such that there is no CR advection) on a domain of  $[-1, 1]^2$ .

Following the setup in [Pakmor et al. \(2016a\)](#), we set initial conditions for the CR energy density to be

$$\epsilon_c(x, y) = \begin{cases} 12 & \text{if } 0.5 < r < 0.7 \text{ and } |\phi| < \frac{\pi}{12} \\ 10 & \text{else,} \end{cases} \quad (\text{A1})$$

where the radial coordinate  $r = \sqrt{x^2 + y^2}$ ,  $\phi = \text{atan2}(y, x)$ , and the diffusion coefficient is set as  $\kappa_c = 0.01$ .

In [Figure 14](#), we compare the performance of our anisotropic diffusion implementation against the analytic solution given by

$$\epsilon_c(x, y) = \left\{ 10 + \text{erfc} \left[ \left( \phi + \frac{\pi}{12} \right) \frac{r}{D} \right] - \text{erfc} \left[ \left( \phi - \frac{\pi}{12} \right) \frac{r}{D} \right] \right\} \quad (\text{A2})$$

where  $D = \sqrt{4\kappa_c t}$ .  $\epsilon_c(x, y) = 10$  everywhere else.

After evolving this simulation for 10 code time units, we see the initial wedge of uniform CR energy density moving down its gradient around the magnetic fields lines. The lower resolution runs have lower peak values of CR energy density and show signs of CR transport perpendicular to the magnetic field direction. Both of these properties improve with increased resolution. The best-resolved simulation (800 x 800, fixed grid) matches the analytic solution well.

At a later time ( $t = 100$  code units), the CR energy density has reached the opposite side of the circle traced by the toroidal magnetic field lines. The energy density approaches a steady state and is nearly evenly distributed around the annulus. In

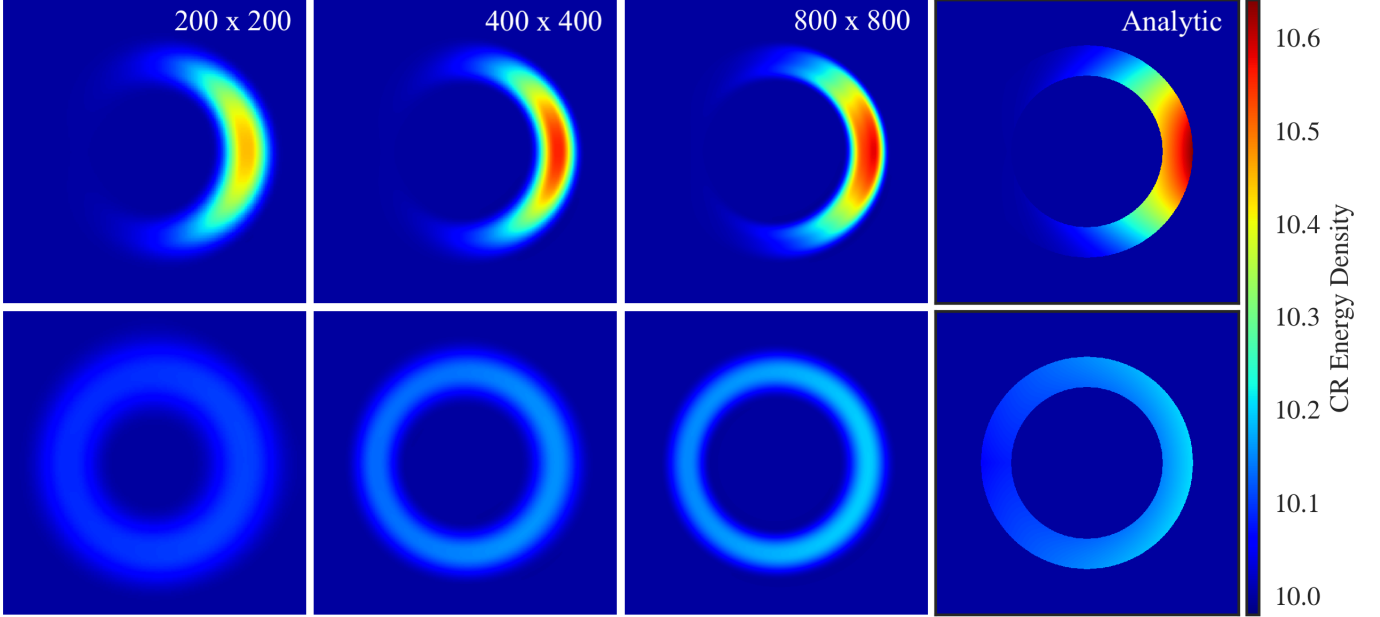


FIG. 14.— A 2D test of anisotropic diffusion of CR energy density along circular magnetic field lines at an early time ( $t = 10$ ; top row) and a late time ( $t = 100$ ; bottom row). The columns are ordered from left to right by increasing resolution, ending with the analytic solution. With anisotropic diffusion, CRs are confined to propagate solely along magnetic field lines. Increasing resolution decreases the amount of diffusion perpendicular to the magnetic field.

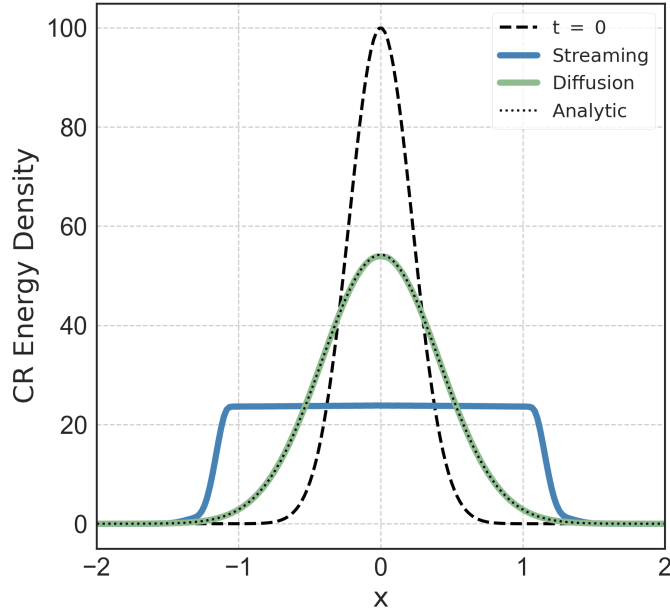


FIG. 15.— A comparison of the time evolution of a 1D Gaussian profile with CR streaming (green) and diffusion (blue). A magnetic field of strength 0.25 code units lies in the  $x$  direction. The analytic solution for the CR diffusion profile is overlotted as a black dotted line. Although no analytic solution exists for the CR streaming case, our results qualitatively match previous studies.

low-resolution runs, the average final CR energy is lower, due to conservation of CR energy in the thicker rings.

#### *Streaming*

We test the behavior of our CR streaming implementation with a 1D simulation of an initial Gaussian profile of CR energy density (see Figure 15). The initial CR energy density profile is set by

$$\varepsilon = \varepsilon_0 e^{-x^2/2D}, \quad (\text{A3})$$

where  $x$  is the spatial coordinate. In our example, we chose constants  $\varepsilon_0 = 100$  and  $D = 0.05$ . We include a magnetic field in the  $\hat{x}$  direction of a strength of 0.25 in code units. We isolate the effects of CR streaming and diffusion by fixing the gas so that no

advection is taking place.

For CR diffusion, the analytic solution for the evolution of the CR energy density over time is given by

$$\varepsilon = \varepsilon_0 \sqrt{\frac{D}{D + 2\kappa_\varepsilon t}} \exp\left(\frac{-x^2}{2(D + 2\kappa_\varepsilon t)}\right). \quad (\text{A4})$$

The CR diffusion implementation follows the analytic solution well. Although there is no analytic solution for the CR streaming case, our results are qualitatively comparable to previous studies (e.g., [Uhlir et al. \(2012\)](#); [Wiener et al. \(2017\)](#)).